COSMOS-Web: star formation along the early Hubble sequence and the evolution of dust over the redshift range 0 ⊲ z < 12

Citation for the original published paper (version of record):
Eales, S., Smith, M., Bakx, T. et al (2026). COSMOS-Web: star formation along the early Hubble sequence and the evolution of dust over the
redshift range 0 ⊲ z < 12. Monthly Notices of the Royal Astronomical Society, 550(1).
http://dx.doi.org/10.1093/mnras/stag1000

Monthly Notices of the ROYAL ASTRONOMICAL SOCIETY

MNRAS **550,** 1–28 (2026)
Advance Access publication 2026 May 29
https://doi.org/10.1093/mnras/stag1000

COSMOS-Web: star formation along the early *Hubble* sequence and the evolution of dust over the redshift range $0 < z < 12$

Stephen Eales,[1★] Matthew W. L. Smith [1] Tom Bakx [2] Jordan C.J. D'Silva,[3] Feng-Yuan Frey Liu [4] and Aparna Venkateshwaran[1]

[1]*Cardiff Hub for Astrophysics Research and Technology (CHART), School of Physics and Astronomy, Cardiff University, 5 The Parade, Cardiff CF24 3AA, UK*
[2]*Department of Space, Earth and Environment, Chalmers University of Technology, Chalmersplatsen, SE-4 41296 Gotherburg, Sweden*
[3]*International Centre for Radio Astronomy Research (ICRAR), University of Western Australia, Crawley, WA 6009, Australia*
[4]*Institute for Astronomy, University of Edinburgh, Royal Observatory of Edinburgh, Blackford Hill, Edinburgh EH9 3HJ, UK*

Accepted 2026 May 18. Received 2026 May 13; in original form 2025 December 12

ABSTRACT

We have carried out a stacking analysis with the COSMOS-Web catalogue on one of the deepest ever SCUBA-2 images at 850-μm, allowing us to estimate the mean submillimetre flux density for samples of galaxies split by stellar mass and morphological class over the redshift range $0 < z < 12$. For all morphological classes, the mean star formation rate estimated from the dust emission increases with redshift, reaching a value for the most massive galaxies ($M_* \simeq 10^{11}$ M$_\odot$) of $\gtrsim 80$ M$_\odot$ yr^{-1} at $2 < z < 4.5$. In this redshift range, the mean star formation rate for these galaxies falls along the *Hubble* sequence from $\simeq 280$ M$_\odot$ yr^{-1} for irregular galaxies at one end to $\simeq 80$ M$_\odot$ yr^{-1} for spheroids at the other end, which shows that quenching was already happening shortly after the emergence of the *Hubble* sequence. We also show that the transformation of 'submillimetre galaxies' can reproduce the growth in number density of massive bulge-dominated and spheroidal galaxies over the redshift range $1.5 < z < 4$. As a side project, we have used our stacking results to determine the relationship between the mean density of dust and redshift in the range $0 < z < 12$. We show that a chemical evolution model based on the 'star formation history' of the universe, with a gas outflow rate equal to the star formation rate, can explain the monotonic rise with redshift in the dust-to-stellar mass ratio and reproduce the relationship between mean dust density and redshift remarkably accurately.

Key words: galaxies: evolution – galaxies: high-redshift – submillimetre: galaxies.

1 INTRODUCTION

The discovery of the 'submillimetre galaxies' (henceforth SMGs) in the first submillimetre surveys was an initial contribution of this new kind of astronomy to our understanding of galaxy evolution (I. Smail, R. J. Ivison & A. W. Blain 1997; A. J. Barger et al. 1998; D. H. Hughes et al. 1998; S. Eales et al. 1999). It is difficult to avoid the conclusion that SMGs are the ancestors of present-day massive ellipticals for two reasons. First, the spectra of present-day massive ellipticals imply that most of their stars were formed $\approx 10 - 12$ Gyr ago in bursts lasting $\simeq 5 \times 10^8$ yr (D. Thomas et al. 2005, 2010), and SMGs are the only galaxies that we know of that are at the right epoch with high enough star formation rates (S. E. Scott et al. 2002; S. J. Lilly et al. 2013; J. M. Simpson et al. 2017; U. Dudzevičiūtė et al. 2020). Second, galaxies in the universe today with stellar masses $> 2 - 3 \times 10^{11}$ M$_\odot$ are almost entirely ellipticals (L. S. Kelvin et al. 2014), and the masses of the SMGs are already so high (J. M. Simpson et al. 2017; S. Eales et al. 2024) that it is hard to imagine what else they could turn into.

The surveys with the *James Webb Space Telescope* (*JWST*; C. M. Casey et al. 2023; S. L. Finkelstein et al. 2025; D. P. Stark et al. 2026) are now discovering galaxies well beyond the epoch of the SMGs ($2 < z < 6$), galaxies that must be at an early stage of evolution simply because of the limited time since the big bang. Submillimetre observations are still vital for studying this even earlier population because without them it is easy to underestimate the rate at which stars are forming in these galaxies. Attempts to estimate a galaxy's star formation rate by fitting population synthesis models to its ultraviolet (UV)-to-near-infrared (IR) spectral energy distribution (SED) tend to fail when the dust obscuration is too high, even though this method makes an attempt to correct for the effect of dust. The SMGs are an extreme example, since the typical visual extinction from SED fitting is ~ 2.5 mag (J. McKinney et al. 2025), whereas the estimates from submillimetre continuum observations of the dust are ~ 400 mag (J. M. Simpson et al. 2017; U. Dudzevičiūtė et al. 2020; K. C. Harrington et al. 2021), but recent work suggests this may be a problem for galaxies with star formation rates as low as 100 M$_\odot$ yr^{-1} (F.-Y. Liu et al. 2026).

★ E-mail: steve.a.eales@gmail.com

If SMGs are destined to become massive elliptical galaxies, they still have a long way to go. From a chemical point of view, they are already at an advanced evolutionary stage because, based on observations of the dust, CO, and [C I], a typical SMG at $z \sim 4$ already contains a mass of metals equal to the entire metal content (in the gas and stars) of a massive early-type galaxy today (S. Eales et al. 2024). But since they have very high star formation rates and either irregular or disc-dominated structures (C.-C. Chen et al. 2022; C. Cheng et al. 2023; S. Gillman et al. 2024; J. McKinney et al. 2025), they have undergone neither the 'quenching' of the star formation nor the morphological transformation necessary to turn them into a massive elliptical galaxy.

The causes of morphological transformation and quenching are, of course, two of the big unknowns in our understanding of galaxy evolution in general and are two of the themes of this paper. The two main processes that have been suggested for creating the structures of elliptical galaxies are galaxy merging (A. Toomre & J. Toomre 1972; P. F. Hopkins et al. 2008) or the collapse of gas with low angular momentum (G. L. Granato et al. 2004; H. Übler et al. 2014). The processes suggested as the cause of the quenching are more varied, including a merger-triggered starburst (P. F. Hopkins et al. 2008), radiative-mode (A. C. Fabian 2012; F. Bollati et al. 2024) or radio-mode (D. J. Croton et al. 2006; Y. Dubois et al. 2016) AGN (active galactic nucleus) feedback, some other 'starvation'/'strangulation' process (R. B. Larson, B. M. Tinsley & C. N. Caldwell 1980; Y. Peng, R. Maiolino & R. Cochrane 2015), stabilization of the gas in a disc by the growth of a bulge (M. Martig et al. 2009), or some environmental process (Y.-j. Peng et al. 2010) that strips away the gas such as ram-pressure stripping. In this paper (as in the literature), we often casually refer to both the reduction in the star formation rate or the removal of a galaxy's gas as 'quenching', since for most of the processes above these are the same thing, but it is important to note that if disc-stabilization (M. Martig et al. 2009) is the cause, a galaxy's gas reservoir may stay full even though the star formation rate drops.

The morphological transformation and quenching do not necessarily happen at the same time or on the same time-scale. In principle, it is possible to observationally separate these two processes, because different combinations in the lists above make different predictions about the temporal relation between the morphological transformation and the quenching.

Suppose, for example, that the emergence of an elliptical galaxy is the result of the merging of two galaxies with the merger triggering a starburst that rapidly depletes the gas (P. F. Hopkins et al. 2008). When we look back to the epoch at which ellipticals emerge, we would expect to find them already with low star formation rates and largely depleted of gas. This would also be the case if the infall of gas into the centre of the new galaxy as the result of the merger led to the formation of an AGN, which then expelled the gas through radiative-mode feedback (P. F. Hopkins et al. 2008). On the other hand, if the morphological transformation was accomplished by merging but the quenching occurred later more slowly as the result of starvation by radio-mode feedback or some other means (R. B. Larson et al. 1980; D. J. Croton et al. 2006; Y. Peng et al. 2015), we would expect to find high-redshift ellipticals that still have high star formation rates and large gas reservoirs.

Before the era of *JWST* and *Euclid*, this simple test was hard to perform because of the limited information about the morphologies of high-redshift galaxies, largely confined to the morphologies measured with the *Hubble* CANDELS survey (S. Wuyts et al. 2011). In those days, the standard approach was to try to measure the gas content of high-redshift quiescent galaxies, on the assumption that these are mostly early-type galaxies, for which there was fairly good evidence (S. Wuyts et al. 2011; R. Gobat et al. 2018). The standard technique used to estimate the gas mass of a galaxy was to measure the dust mass, and so infer the gas mass, since dust has major advantages over CO for tracing the molecular phase in galaxies (S. Eales et al. 2012; G. E. Magdis et al. 2012; N. Scoville et al. 2014; L. J. Tacconi, R. Genzel & A. Sternberg 2020; L. Dunne et al. 2022). This approach had contradictory results, with some statistical studies (R. Gobat et al. 2018; G. E. Magdis et al. 2021) finding that the dust masses of massive quiescent galaxies are higher at $z \sim 1 - 2$ than they are today, although not as high as those of star-forming galaxies at the same redshift, and other studies (K. E. Whitaker et al. 2021) finding much lower dust masses.

The advent of *JWST* and *Euclid* has changed this field completely, making it possible to classify the morphologies of galaxies over large areas of the sky (M. Huertas-Company et al. 2025; Euclid Collaboration 2025a). These studies are rapidly advancing our understanding of galaxy evolution. Observations with *Euclid* have already shown that the common assumption of there being two basic classes of galaxies – quiescent/early-type and star-forming/late-type – is too simplistic, since in a study of the morphologies of nearly a million galaxies in the redshift range $0.25 < z < 1$, only 82 per cent fell in the standard categories, with 13 per cent of the galaxies consisting of star-forming spheroids and 5 per cent of quiescent discs (Euclid Collaboration 2025b). Observations with *JWST* have shown that the familiar morphologies of the Hubble sequence seem to emerge at $z \sim 4$, with galaxies at higher redshift either being unresolved or classified as irregular (M. Huertas-Company et al. 2025).

In this paper, we use morphological classifications from the *JWST* COSMOS-Web survey (C. M. Casey et al. 2023; M. Shuntov et al. 2025a) to make measurements of the submillimetre emission from dust for samples of galaxies split by stellar mass, redshift and, for the first time, morphological class, which allows us to directly address the issue of whether morphological transformation is linked to the quenching of the star formation. Although it is possible to measure the submillimetre emission from individual galaxies with interferometers such as the Atacama Large Millimeter/Submillimeter Array (ALMA), it is very challenging to do this for large numbers of galaxies. For this reason, we have used one of the deepest ever submillimetre surveys carried out with a single-dish telescope, the James Clerk Maxwell Telescope (JCMT), mitigating the effect of the poor resolution (relative to the *JWST* and *Euclid*) by carrying out a 'stacking analysis' in which we measure the mean submillimetre flux density for samples of galaxies rather than individual galaxies.

As a second science project, we have also used our stacking results to investigate the general properties of dust in the universe. This paper is a follow-up to S. Eales & B. Ward (2024), in which we used a submillimetre stacking analysis for the galaxies in the COSMOS survey (N. Scoville et al. 2007) to determine how the mean density of dust in the universe depends on redshift out to $z \sim 5.5$. Although COSMOS-Web does not cover as large a field of view as COSMOS ($\sim 0.54\ \mathrm{deg}^2$), it is still the largest *JWST* survey and thus the one least affected by cosmic variance. The release of its data (M. Shuntov et al. 2025a) has allowed us to extend our investigation of dust in the universe out to $z \sim 12$.

The paper is organized as follows: Section 2 describes our methods; Section 3 gives our results; Section 4 is the discussion; and our results and conclusions are summarized in Section 5. Given that this is such a long paper, we note that for those primarily interested in galaxy evolution the key results are in Sections 4.1–4.4, and 4.6. For those primarily interested in the evolution of dust, the key results are in Sections 3.4, 3.5, and 4.5.

We use the cosmological parameters given in Planck Collaboration XIII (2016).

2 METHODS

2.1 Overview

The basic technique used in this paper is 'stacking'. In a stacking analysis, measurements of the flux density of a sample of galaxies are used to calculate the weighted-mean flux density for the sample, which is a very useful technique when many of the individual measurements have low signal-to-noise ratio. In our study, we have carried out a stacking analysis using the images from the S2COSMOS (SCUBA-2 COSMOS survey) 850-µm survey of the COSMOS field (J. M. Simpson et al. 2019).

2.2 The submillimetre image

The 850-µm image was constructed using 640 h of new and archival observations taken with the SCUBA-2 camera on the JCMT as part of the S2COSMOS survey. It achieved a median noise level of $\sigma_{850\ \mu\mathrm{m}} = 1.2$ mJy beam^{-1} over 1.6 sq deg which covers the COSMOS-Web region (J. M. Simpson et al. 2019). The angular resolution of the image is ≃15 arcsec (FWHM, full width at half-maximum).

2.3 The COSMOS-Web samples

Our samples were taken from the COSMOS-Web catalogue,[1] described by M. Shuntov et al. (2025a). We only used objects from the catalogue if they had warn_flag = 0 [2], removing problematic objects such as those suspected of being hot pixels, or those with inconsistencies between the JWST and ground-based photometry.

In our analysis, we used the estimates of the photometric redshift (`zfinal`), stellar mass (`mass_med`), and specific star formation rate (`ssfr_med`) in the COSMOS-Web catalogue, which were obtained with the LEPHARE (Photometric Analysis for Redshift Estimate) code for fitting SEDs (S. Arnouts et al. 1999), which is based on models of the stellar population of a galaxy (G. Bruzual & S. Charlot 2003). We restricted our analysis to galaxies with stellar masses in the range $9.0 < \log_{10}M_* < 11.5$ and redshifts in the range $0.2 < z < 12$. We chose the lower mass limit because this is the approximate stellar mass completeness limit of COSMOS-Web (M. Shuntov et al. 2025a).[3] We chose the upper mass limit because high-redshift galaxies at higher masses are likely to be spurious, the effect of Eddington bias (C. M. Casey et al. 2024). To be consistent with estimates of the COSMOS-Web stellar mass function, we removed objects at $z > 3.5$ for which there is evidence that they are either AGN or 'little red dots' using the same selection criteria as used in calculating the stellar mass function (M. Shuntov et al. 2025a). After removing these, our base sample consisted of 102 549 galaxies.

In our initial analysis, we divided the galaxies into 14 redshift intervals (Table 1) over the redshift range $0 < z < 12$ and five equal intervals of log stellar mass (M_*) over the range $9.0 < \log_{10} M_* < 11.5$. This gave us 70 different samples of galaxies, the goal of the stacking being to produce an unbiased estimate of the mean 850-µm flux density of each sample.

At a later stage in the analysis, we also divided the galaxies into morphological types. We used the morphological classifications given in the ML-MORPHO extension of the COSMOS-Web catalogue. These were obtained by using a machine-learning algorithm trained on the *Hubble* CANDELS survey to classify the COSMOS-Web galaxies into four broad morphological classes: spheroids, bulge-dominated, disc-dominated, and irregular (M. Huertas-Company et al. 2025). The catalogue includes three classifications for each galaxy made using images made through three *JWST* filters. We followed M. Huertas-Company et al. (2025) in choosing the morphological classification for each galaxy so they were all done at roughly the same rest-frame wavelength. We used the classifications from the *F*150*W*, *F*277*W*, and *F*444*W* images for the redshift ranges $z < 1$, $1 < z < 3$, and $z > 3$, respectively. Of the sample, ≃ 97 per cent of the galaxies have morphological classifications. The morphological breakdown of each of our 70 samples is given in Appendix A. Although the overall percentage with no morphological classification is very small, it does reach very high values in some of the high-redshift bins. Our investigation of the relationship between star formation rate and morphological type (Sections 4.1–4.4) is therefore restricted to $z < 4.5$. The largest percentage incompleteness below this redshift is 35 per cent for the sample with $3.5 < z < 4.5$ and $11.0 < \log_{10}(M_*) < 11.5$.

Table 1. Redshift ranges of the samples and results from fitting equation (5).

Redshift ranges	a	b
$0.2 < z < 0.5$	-7.1×10^{-4}	8.2×10^{-3}
$0.5 < z < 0.8$	-1.7×10^{-3}	1.9×10^{-2}
$0.8 < z < 1.1$	-1.7×10^{-3}	2.0×10^{-2}
$1.1 < z < 1.5$	-1.6×10^{-3}	1.9×10^{-2}
$1.5 < z < 2.0$	-2.7×10^{-3}	3.1×10^{-2}
$2.0 < z < 2.5$	-3.7×10^{-3}	4.4×10^{-2}
$2.5 < z < 3.0$	-4.8×10^{-3}	5.6×10^{-2}
$3.0 < z < 3.5$	-3.7×10^{-3}	4.5×10^{-2}
$3.5 < z < 4.5$	-6.6×10^{-3}	7.9×10^{-2}
$4.5 < z < 5.5$	-3.7×10^{-3}	5.1×10^{-2}
$5.5 < z < 6.5$	-5.2×10^{-3}	6.8×10^{-2}
$6.5 < z < 7.5$	-4.5×10^{-3}	5.7×10^{-2}
$7.5 < z < 8.5$	-5.5×10^{-3}	7.3×10^{-2}
$8.5 < z < 12.0$	...	...

2.4 Stacking – general points

Although the relatively poor angular resolution of the SCUBA-2 image (FWHM of 15 arcsec) means there are many *JWST* galaxies within each resolution element, stacking will produce an unbiased estimate of the mean flux density of a sample as long as the mean of the image is zero and there is no clustering between

[1] Public data release: COSMOS-Web DR1

[2] A detailed description of how the data were flagged is included in the public data release page.

[3] COSMOS Web is ≃ 80 per cent complete to this stellar mass at $z \sim 10$ (M. Shuntov et al. 2025b)

galaxies (G. Marsden et al. 2009; M. P. Viero et al. 2012). Two things complicate matters. First, obviously, galaxies are clustered. Second, the redshifts in the COSMOS-Web catalogue are photometric redshifts, which means the galaxies are not necessarily at their correct redshifts.

We attempted to solve the first problem by using the SIMSTACK algorithm (M. P. Viero et al. 2013), which is an elegant way of correcting for the effect on the measurements of clustering between galaxies in different samples. We attempted to correct for the second problem by using a Monte Carlo simulation to estimate the additional errors in the stacked flux densities arising from errors in the redshifts and stellar masses. We generated 100 artificial COSMOS-Web catalogues by using the redshifts and stellar masses in the real catalogue, and the errors on both, to generate bootstrapped sets of stellar masses and redshifts for each artificial catalogue.

We carried out two versions of the stacking analysis. The first version used the basic method, in which we made no attempt to correct for clustering. The second version was the SIMSTACK version. Our reason for doing so was that the results from the basic method gave us a useful check on the results from SIMSTACK. The differences between the two sets of results also gave us insight into the actual effect of clustering on stacking. In the following two subsections, we give some technical details of how we applied the two methods.

2.5 Basic stacking method

In this version of the method, we made no attempt to correct for the clustering between the galaxies in different samples. We simply measured the flux density and noise from the S2COSMOS images for each of the galaxies in a sample, and then calculated the mean flux density for the sample, with the weight for each galaxy, w_i, given by:

$$w_i = \frac{\frac{1}{\sigma_i^2}}{\sum_i \frac{1}{\sigma_i^2}} \quad (1)$$

in which σ_i is the noise for the galaxy and the sum is over all the galaxies in the sample. In this method, we used the S2COSMOS image and corresponding noise image that had been smoothed with a filter equal to the point spread function of the observations to maximize the signal-to-noise ratio.

To calculate the error on the stacked signal that is as close as possible to ground truth, we carried out a Monte Carlo simulation for each sample. If there were $N_{\rm gal}$ galaxies in the sample, we generated 1000 sets of $N_{\rm gal}$ random positions. We then carried out a stacking analysis for each set. We used the variance of the 1000 weighted mean values to estimate the error in the stacking analysis: $\sigma_{\rm stack}$.

As described above, we also produced 100 artificial versions of the COSMOS-Web catalogue, using the photometric redshifts and the stellar masses and their associated errors to generate a set of bootstrapped redshifts and stellar masses for each artificial catalogue. We carried out the same stacking analysis for each artificial catalogue, using the variance of the results to calculate the error that arises from the errors in the redshifts and the stellar masses: σ_{JWST}. We added $\sigma_{\rm stack}$ and σ_{JWST} in quadrature to get the final error on the stacked signal.

To produce a more visual way of judging the significance of the stacked signal, we generated images that show the signal-to-noise ratio of the mean 850-μm flux density of each sample. Each image is produced from a 23 × 23 array of offsets from the *JWST* positions centred on (0,0) and with a grid spacing of 2 arcsec. The image value at each pixel is the signal-to-noise ratio of the mean 850-μm flux density produced by the stacking analysis when the galaxies are placed at this offset from their true positions. The upper panel of Fig. 1 shows these signal-to-noise images.

2.6 Stacking using SIMSTACK

In this version, we used the SIMSTACK algorithm (M. P. Viero et al. 2013, 2022). The SIMSTACK algorithm fits the contribution to the submillimetre image from all samples simultaneously, which means it is not biased by the effect of clustering between galaxies in different samples. There is a particularly clear exposition of the maths of the algorithm in Euclid Collaboration (2025c). The implementation of the algorithm that we used in this paper is the one available at SIMSTACK3.

We followed the same procedure as described in M. P. Viero et al. (2022). In this case, we used the unconvolved S2COSMOS images. As the result of the errors in the photometric redshifts, there will be a contribution to the stacked signal from clustering between galaxies that are in samples in different redshift intervals. We therefore followed M. P. Viero et al. (2022) in applying SIMSTACK to samples at all redshifts simultaneously. We included an additional sample in the SIMSTACK analysis that consisted of all the galaxies in the COSMOS-Web catalogue outside the mass and redshift limits of the other 70 samples. To avoid errors being produced by holes in the coverage of the COSMOS-Web catalogue, we included a flat foreground layer in SIMSTACK (M. P. Viero et al. 2022).

As in the other version of the stacking, we applied SIMSTACK to the 100 artificial versions of the COSMOS-Web catalogue to estimate the error produced from the errors in the photometric redshifts and stellar masses: σ_{JWST}. We added this error in quadrature to the error produced by SIMSTACK, $\sigma_{\rm stack}$, to get the final error on the mean flux density.

As in the other stacking method, we produced cutout images showing the signal-to-noise ratio for each sample, which we generated using the method described in the previous section. These are shown in the lower panel of Fig. 1.

2.7 The temperature models

Both the stacking methods above produce an estimate of the mean submillimetre flux density at a single wavelength. They do not produce an estimate of the temperature of the dust, which is essential for an accurate estimate of the mass of dust. In a similar way, it is only possible to estimate the total (bolometric) emission of the dust, which can be used to estimate the galaxy's star formation rate (R. C. Kennicutt 1998; R. C. Kennicutt & N. J. Evans 2012), if one knows the temperature of the dust or, equivalently, has a model of the SED of the dust emission. The accuracy of the estimates of both, of course, depend critically on the accuracy of the assumptions about the dust temperature or the SED.

There is no consensus about whether the temperature of the dust in galaxies does generally increase with redshift, with evidence both for (G. E. Magdis et al. 2012; B. Magnelli et al. 2014; M. Béthermin et al. 2015; R. J. Ivison et al. 2016; A. L. Faisst et al. 2017; C. Schreiber et al. 2018; R. Bouwens et al. 2020; M. P. Viero et al. 2022; J. Witstok et al. 2023) and against this (A. M. Swinbank et al. 2014; C. M. Casey et al. 2018; S. Jin et al. 2019; U. Dudzevičiūtė et al. 2020; P. M. Drew & C. M. Casey 2022;

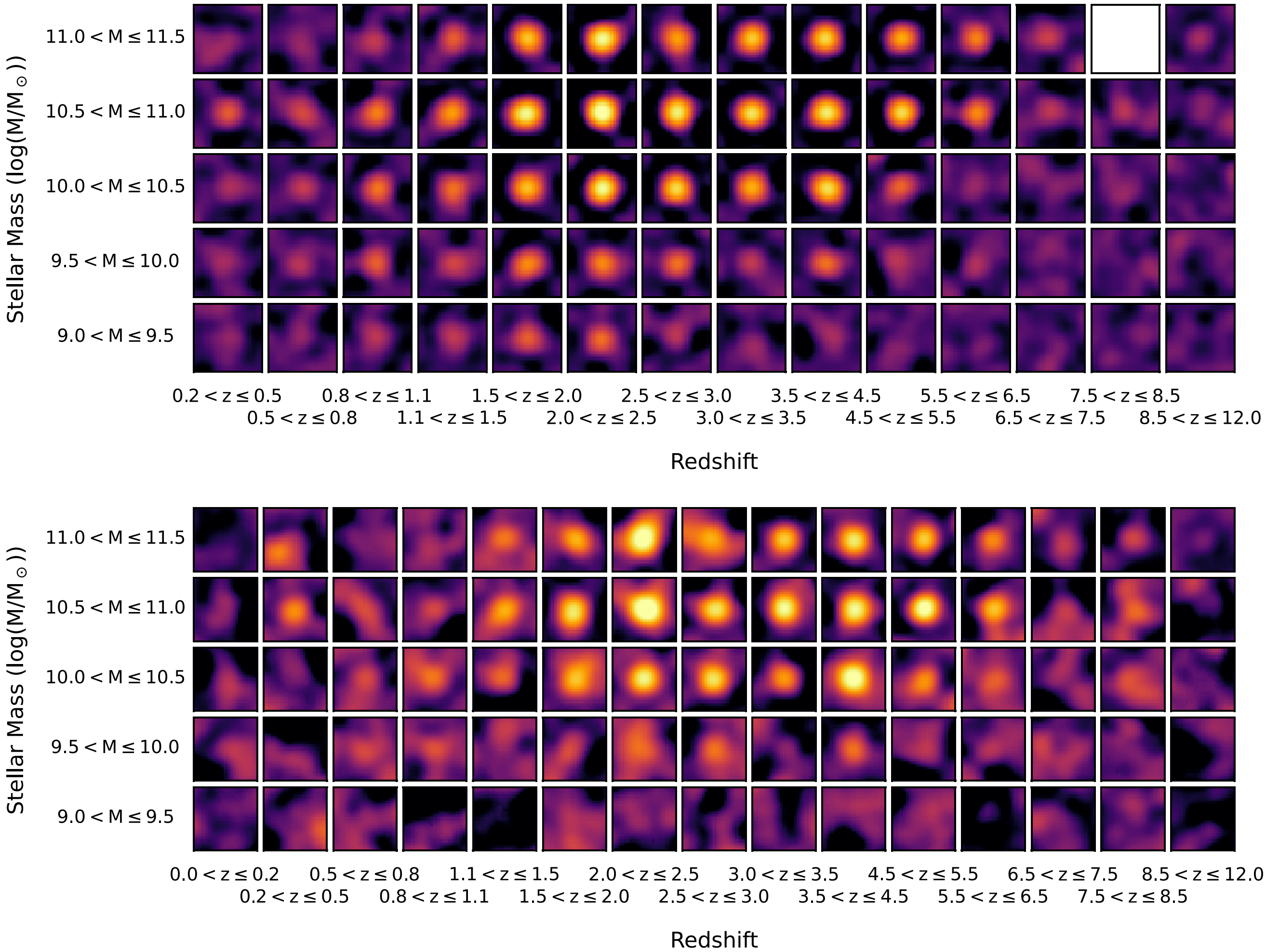

Figure 1. Images showing the signal-to-noise ratio of our measurements of the mean 850-μm flux density of 70 samples of galaxies, with the results from the basic stacking method shown above and from SIMSTACK shown below. The annotation shows the redshift and mass range for each sample. Each pixel in each image represents a different offset from the COSMOS-Web positions, with the zero-offset position being in the centre. The images are squares with a side of 44 arcsec and a pixel size of 2 arcsec. The blank field in the top panel is for a sample containing less than four galaxies, the minimum number for our basic stacking method.

G. J. Bendo et al. 2023; B. A. Ward et al. 2024). The increase in the temperature of the cosmic microwave background radiation (CMB) at high redshift does mean that there will be some increase in the dust temperature (E. da Cunha et al. 2013), but the lack of evolution claimed in the studies above generally refers to the temperature the dust would be at in the absence of the CMB, e.g. B. A. Ward et al. (2024).

There is a well-known bias that when a single modified blackbody is fitted to a set of far-IR/submillimete photometry for a galaxy, the measured temperature – the luminosity-weighted temperature – is always higher than the mean mass-weighted dust temperature (S. A. Eales, C. G. Wynn-Williams & W. D. Duncan 1989; L. Liang et al. 2019), which is what one needs to know for an accurate estimate of the dust mass. The reason for this is that there is always a mixture of dust at different temperatures in a galaxy, and since warm dust radiates more strongly, and at a shorter wavelength, than the same mass of cold dust, the measured, luminosity-weighted, temperature is always biased high. For a given set of observation wavelengths, this bias increases with redshift, since as the redshift increases, the part of the galaxy's rest-frame SED covered by the observation set will move to shorter wavelengths. The problem is not as bad for an estimate of the bolometric luminosity of the dust, since the measured, luminosity-weighted, temperature is much closer to what one needs for an accurate estimate of the bolometric luminosity.

In Appendix B, we show that this same bias applies to temperature measurements from stacking analyses, which sometimes show dramatic increases in dust temperature with redshift (M. P. Viero et al. 2022). We show that this bias is present even if all the individual galaxies in the stacking sample only contain dust at a single temperature. For this reason, the temperature models below are based on observations of individual galaxies rather than estimates in the literature of the dust temperature from stacking analyses.

We have explored the sensitivity of our estimates of dust mass and bolometric dust luminosity using three temperature models:

(i) *Cold.* In this model, we assume that the mean mass-weighted dust temperature is 22 K and does not change with redshift, which is the assumption we made in our previous paper (S. Eales & B. Ward 2024). This is the median dust temperature found from the fits of a single modified blackbody to the flux densities for ∼80 000 galaxies found in the *Herschel* ATLAS survey (S. Eales & B. Ward 2024). There was no evidence in this study for any variation of dust temperature with redshift out to $z \simeq 1$. Despite the disagreement between the observational studies, cosmological simulations have shown that at higher redshifts, while the observed, luminosity-weighted, dust temperature does increase with redshift, the mass-weighted dust temperature does not (L. Liang et al. 2019). We therefore assume in this model that there is no evolution in the dust temperature.

(ii) *Star-former.* The first model must be, at least, a simplification of the situation in real galaxies, because unless a galaxy contains no newly formed stars and no active nucleus, it must contain some phase of warmer dust. The galaxies that seem likely to contain the highest fraction of warm dust are the luminous dusty star-forming galaxies, which are often labelled as ultraluminous IR galaxies at low redshift and SMGs at high redshift. Models of the SEDs that include two modified blackbodies at different temperatures have shown that although the galaxies in these classes do contain some warm dust, most of the dust is at a low temperature (L. Dunne & S. A. Eales 2001; E. A. Pearson et al. 2013; T. J. L. C. Bakx et al. 2018). As our second model, we have adopted the model of T. J. L. C. Bakx et al. (2018), who found that the average SED of the most luminous SMGs at $z > 2$ could be represented by a mixture of dust at 21.3 and 45.8 K, with the ratio of the mass of cold dust to warm dust being 26.6. Since this is very similar to the results for low-redshift ultraluminous IR galaxies (L. Dunne & S. A. Eales 2001), we include no evolution in this model.

(iii) *Evolve.* This model is based on the dust temperatures measured for 17 galaxies over the redshift range $4 < z < 8$ (J. Witstok et al. 2023), which do show an increase of the dust temperature with increasing redshift. The relationship matches well the prediction from cosmological simulations for the relationship between the observed, luminosity-weighted, dust temperature and redshift (L. Liang et al. 2019). We have used the relationship predicted from the cosmological simulations as our model, with the small modification that we have used a temperature of 23 K on the left-hand side of the relationship, rather than the 25 K found in the simulations (L. Liang et al. 2019), in order to make it consistent with our first two models at low redshift:

$$\log_{10}\left(\frac{T_{\rm dust}}{23\ {\rm K}}\right) = -0.02 + 0.25\log_{10}(1+z) \quad (2)$$

We note that although this relationship shows evolution and matches well the observations of the high-redshift sample (J. Witstok et al. 2023), the same simulations predict that although the measured, luminosity-weighted, dust temperature does change with redshift, the mass-weighted dust temperature, which is what we really want, does not change with redshift (L. Liang et al. 2019).

We believe the model that is likely to be closest to the truth is star-former, since it is based on a more sophisticated model than a single modified blackbody, making it less susceptible to the temperature bias described above, and is an empirical fit to the SEDs of real star-forming galaxies. We have included the other two models to show the effect on the dust masses of the range of dust temperatures claimed in the literature.

The models above describe the temperature of the dust in the absence of the effect of the CMB. We combined the temperature model and the effect of the CMB as follows. At each redshift, we used the model to estimate the temperature the dust would have in the absence of the CMB. We used eqs (12) and (18) in E. da Cunha et al. (2013) to calculate the actual temperature of the dust and to correct the observed flux density for its suppression in the presence of the CMB. In the case of star-former, we corrected the temperature and flux density for each component separately and then added them to produce the final flux. In calculating dust masses for this model (Section 3.3), we calculated the dust mass for each component separately and then added them to produce the final dust mass. The corrections can be very large. For cold, which is the most extreme case, the correction factors for the flux density are 1.04, 1.91, and 16.8 at $z = 3$, 7, and 12, respectively.

Finally, in this section, we discuss the effects of using these different models on our estimates of dust mass and bolometric dust emission, which we use in Section 4 to estimate the star formation rate. Cold and star-former both yield very similar estimates of the dust mass because in the former all the dust and in the latter 96 per cent of the dust mass is at $T \simeq 20$ K. The two models, though, yield very different estimates of the bolometric dust luminosity because the small percentage of warm dust in star-former vastly out-radiates the 96 per cent of the dust that is cold. The estimates of the dust mass from evolve are similar to the estimates from the other two models at low redshift where the dust temperatures are similar but get increasingly lower than the other two as the redshift, and therefore the temperature of the dust, increases. The estimates of bolometric dust emission for evolve and star-former are similar at all redshifts because in the case of star-former it is the small percentage of warm dust that is responsible for most of the bolometric dust emission.

3 RESULTS

3.1 Comparison between the results of the two stacking methods

Fig. 1 shows the signal-to-noise images for each sample of galaxies and for each stacking method. Fig. 2 shows mean flux density versus mass for each redshift interval, with the results for the basic stacking method shown in mauve and for SIMSTACK in cyan. The values of the flux density and errors obtained from SIMSTACK are given in Appendix A.

Both figures show fairly good agreement between the results from the two stacking methods. Both methods show that in all redshift intervals there is a increase in flux density with stellar mass, which is itself a useful sense check since we cannot think of any reason why a stacking method would produce a spurious relationship like this and it is what one expects if all galaxies have roughly the same ratio of dust-to-stellar mass.

The differences between the results from the two methods are instructive. First, the SIMSTACK flux densities are almost always slightly lower than those from the basic method, which is what one would expect if galaxy clustering is enhancing the signal measured with the latter method. Second, while Fig. 1 shows that the basic method produces significant detections at $\log_{10}M_* < 10.0$, these mostly disappear in the SIMSTACK results. This is also what one would expect. Suppose there are low-mass galaxies clustered around high-mass galaxies within a SCUBA-2 beam. The mean flux densities of each class will be enhanced but the flux densities of the low-mass galaxies will be proportionately more enhanced. Since the effect of galaxy clustering has been corrected in the SIMSTACK results, these are the ones we use in the rest of the paper.

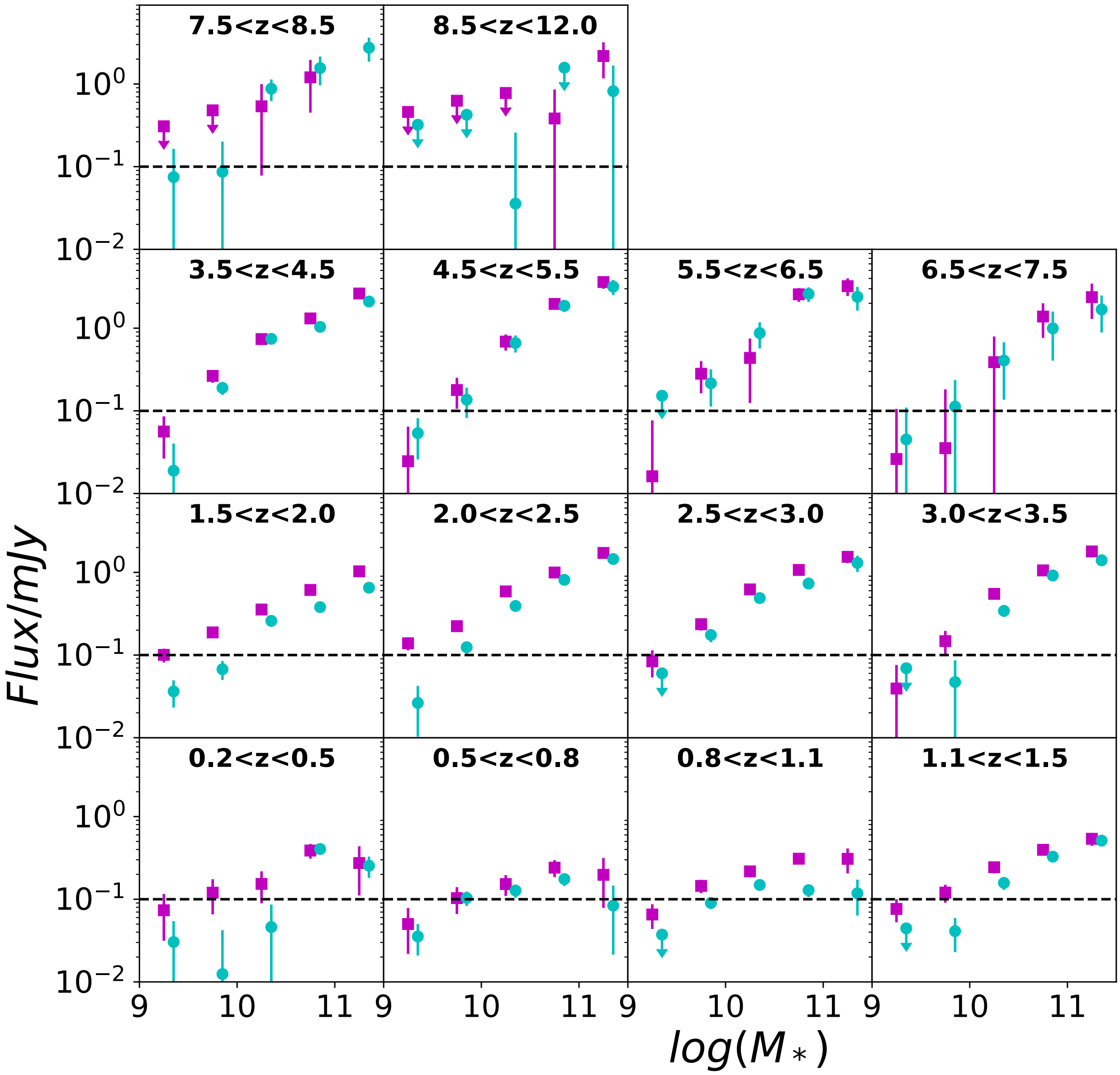

Figure 2. Mean flux density at 850 μm versus mass for each redshift interval. The mauve squares are the values measured with the basic stacking method. The cyan circles are the values measured with SIMSTACK. The two sets have been offset by 0.1 in $\log_{10}(M_*)$, to prevent an overlap. The horizontal dashed line at a flux density of 0.1 mJy has been drawn to aid comparison between the panels. The limits are 3σ upper limits.

3.2 Comparison with previous results

There have been two previous stacking analyses of the S2COSMOS images, which both used SIMSTACK but with galaxy catalogues from ground-based telescopes. Our results are very similar to those of J. M. Simpson et al. (2019). We cannot compare our results precisely with the results of the other study (J. S. Millard et al. 2020) because of the different binning procedure and because the earlier paper did not include the errors on the SIMSTACK fluxes. Although the same trends of flux density with stellar mass and redshift are seen in the two studies, our measurements are lower by ~ 30 per cent than the fluxes in the earlier paper. We do not know the explanation of the difference.

We have made an additional check on our results by comparing them to the results of stacking analyses of massive galaxies with very low star formation rates, 'massive quiescent galaxies'. We divided our samples into star-forming and quiescent galaxies using the LEPHARE estimates (Section 2.1) of the specific star formation rate (star formation rate divided by stellar mass – SSFR). Star-forming galaxies mostly lie on a strip across a diagram of SSFR versus stellar mass, which is often called the 'galaxy main sequence'. We have used a relationship for the evolution of the galaxy main sequence (J. S. Speagle et al. 2014) to divide the galaxies into the two classes, classifying a galaxy as quiescent if its SSFR is at least 1.5 orders of magnitude below a galaxy on the galaxy main sequence with the same stellar mass. We applied the two stacking methods (Sections 2.5 and 2.6) to the two classes, each split into the same 70 bins of stellar mass and redshift as before. In the case of SIMSTACK, we applied the algorithm to all 140 samples simultaneously. We again carried out a Monte Carlo simulation to estimate the errors in the SIMSTACK flux densities arising from the errors in the COSMOS-Web

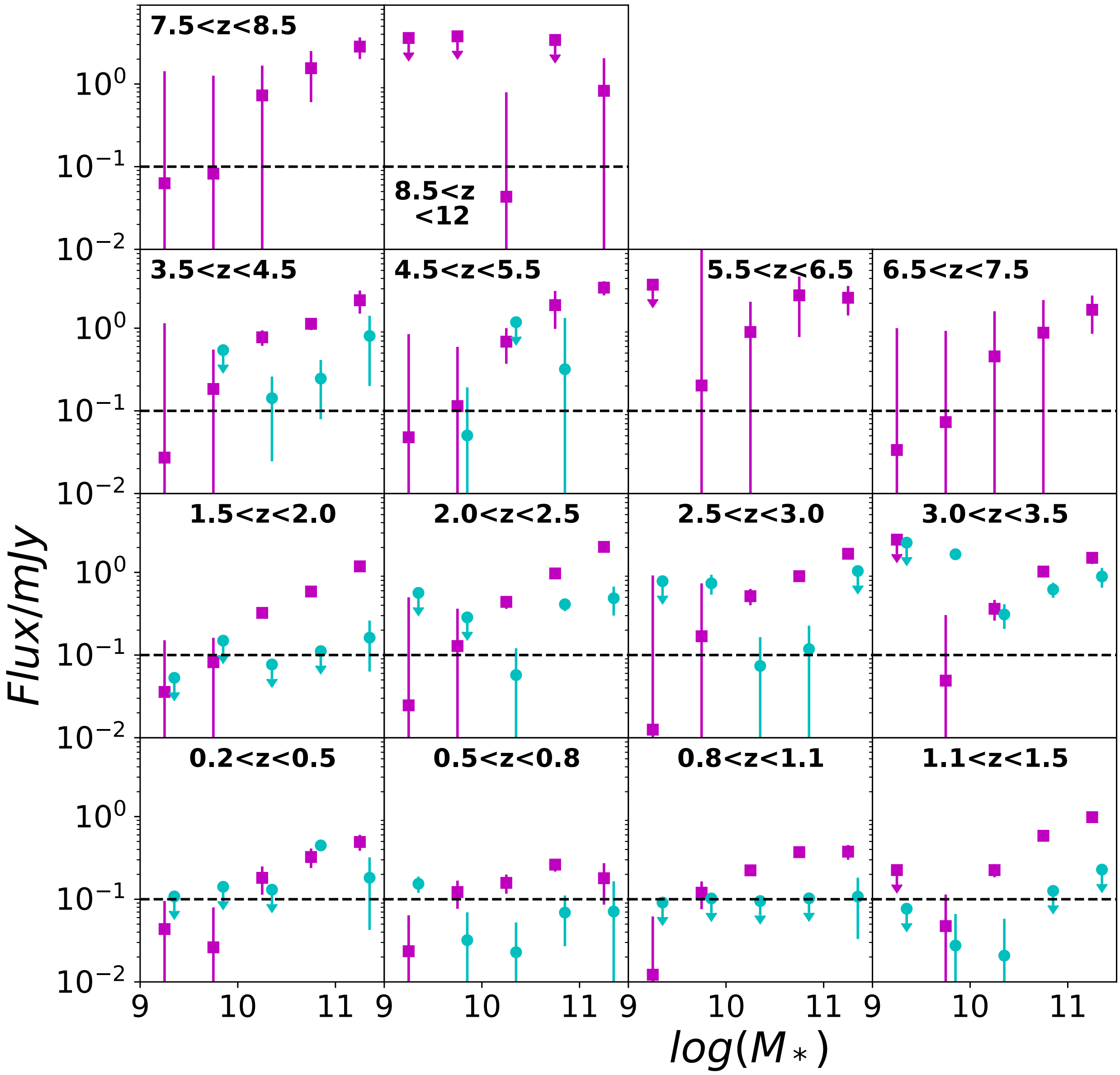

Figure 3. Mean flux density at 850 µm estimated with SIMSTACK (Section 2.4) for star-forming galaxies (mauve squares) and quiescent galaxies (cyan circles) plotted against stellar mass for the 14 redshift intervals. The two sets of points have been offset by 0.1 in $\log_{10}(M_*)$ so that they do not overlap. The horizontal dashed line at a flux density of 0.1 mJy has been drawn to aid comparison between the panels. The upper limits are 3σ upper limits.

photometric redshifts and stellar mass estimates, adding these errors in quadrature to the basic SIMSTACK errors.

Fig. 3 shows the results. The star formation rate and the mass of dust in a galaxy are likely to be correlated because both are correlated with the mass of gas in the galaxy (R. C. Kennicutt 1998; S. Eales et al. 2012). One might therefore expect the submillimetre flux density of the star-forming galaxies to be higher than for the quiescent galaxies in the same redshift and mass interval, and this is what one generally but not always sees in the panels.

In Table 2, we compare our results with other attempts to estimate, through stacking, the mean 850-µm flux density of samples of massive ($M > 10^{11}$ M$_\odot$) quiescent galaxies (R. Gobat et al. 2018; G. E. Magdis et al. 2021). Our estimates are consistent with the previous estimates.

Table 2. Comparison with previous results for quiescent galaxies.

Redshift range	Mean 850-µm flux density	Paper
$z \sim 1.76$	81±23 µJy	R. Gobat et al. (2018)
$1.5 < z < 2.0$	147±102 µJy	This paper
$< z >= 0.5$	100±40 µJy	G. E. Magdis et al. (2021)
$0.2 < z < 0.5$	156±131 µJy	This paper
$< z >= 0.85$	<210 µJy	G. E. Magdis et al. (2021)
$0.5 < z < 0.8$	109±102 µJy	This paper
$< z >= 1.20$	40±30 µJy	G. E. Magdis et al. (2021)
$1.1 < z < 1.5$	55 ±105 µJy	This paper

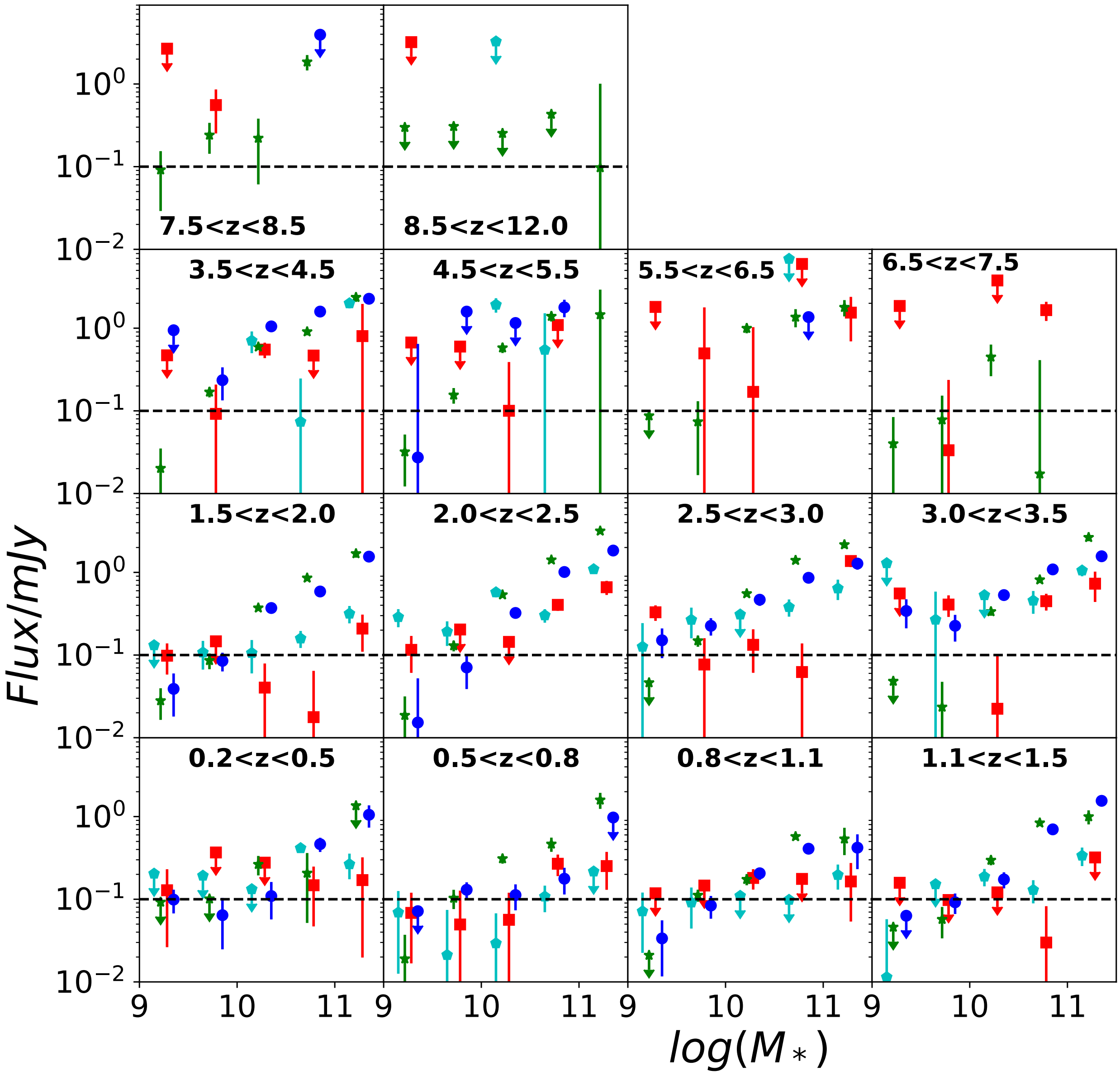

Figure 4. Mean flux density at 850 μm estimated with SIMSTACK for the four different morphological classes from M. Huertas-Company et al. (2025): irregular galaxies – green stars; disc-dominated galaxies – blue circles; bulge-dominated galaxies – cyan pentagons; and spheroids – red squares. The horizontal dashed line at 0.1 mJy has been drawn to aid comparison between the panels. We have added offsets to the sets of points (0.05 in $\log_{10}(M_*)$) to avoid them overlapping. The upper limits are 3σ upper limits.

3.3 The results for different morphological types

We applied the two stacking methods to the four morphological classes: spheroidal, disc-dominated, irregular, and bulge-dominated. We split each class into the same 70 bins of redshift and stellar mass as before. In the case of SIMSTACK, we applied the algorithm to all 280 samples simultaneously. We again carried out a Monte Carlo simulation to estimate the errors in the SIMSTACK results arising from the errors in the COSMOS-Web photometric redshifts and stellar mass estimates, adding these errors in quadrature to the basic SIMSTACK errors.

Fig. 4 shows the results. Today, spheroidal and bulge-dominated galaxies contain less dust than disc-dominated and peculiar galaxies, with spheroidal galaxies, in particular, containing very little dust (M. W. L. Smith et al. 2012). The figure shows that in most panels the submillimetre emission from disc-dominated and irregular galaxies is generally higher than for bulge-dominated and spheroidal galaxies, but the emission from all the morphological categories increases with redshift in roughly the same way. At $z > 4$, the regular *Hubble* sequence has largely vanished (M. Huertas-Company et al. 2025), and the only samples that contain enough galaxies for a measurement are the irregular galaxies.

3.4 The ratio of dust-to-stellar mass

We calculated the mean ratio of dust-to-stellar mass for each of the 70 samples of galaxies in the following way. Starting from the mean flux density for that sample from the SIMSTACK analysis, we estimated the dust mass for each of the galaxies in that sample using the following equation:

$$M_d = \frac{< S_{850\mu\mathrm{m}} > D_L^2}{(1+z)B(\nu_e)\kappa(\nu_e)} \quad (3)$$

in which ν_e is the frequency in the rest frame: $\nu_e = (1+z)\nu_{850\mu\mathrm{m}}$. D_L is luminosity distance, and the dust mass-opacity coefficient, $\kappa(\nu)$, is given by:

$$\kappa(\nu) = \left(\frac{\nu}{\nu_{850\mu\mathrm{m}}}\right)^{\beta} \kappa_{850\mu\mathrm{m}} \quad (4)$$

We assumed a value for β of 2, which is the value found in many recent studies of high-redshift galaxies (E. da Cunha et al. 2021; G. J. Bendo et al. 2023, 2025; D. Ismail et al. 2023; J. Witstok et al. 2023; B. A. Ward et al. 2024), and the widely used value for the mass-opacity coefficient of $\kappa_{850\mu\mathrm{m}} = 0.077\ \mathrm{m}^2\ \mathrm{kg}^{-1}$ (A. James et al. 2002; E. da Cunha, S. Charlot & D. Elbaz 2008; L. Dunne et al. 2011). The value of the mass-opacity coefficient is notoriously uncertain (C. J. R. Clark et al. 2016), but we note that our value was calibrated directly from estimates of the mass of metals in a galaxy (A. James et al. 2002). This makes it an appropriate one to use if one wants to use a model of the evolution of the metals in a galaxy to also model the evolution of the dust, which we do in Section 4.5.

Before calculating the dust mass, we corrected the flux density and the dust temperature for the effect of the CMB (Section 2.7). We calculated the dust mass for all three temperature models: cold, star-former, and evolve (Section 2.7).

Once we had calculated a dust mass for each galaxy in the sample, we calculated the mean value of the ratio of the dust-to-stellar mass for all the galaxies in the sample, using the values of the stellar mass for each galaxy given in the COSMOS-Web LEPHARE catalogue (Section 2.2).

Fig. 5 shows the mean ratio of dust-to-stellar mass versus stellar mass for each of the 14 redshift intervals. The estimates for cold and star-former are fairly similar at all redshifts, but the estimates for evolve are lower than for the other two, with the difference increasing with redshift. For all three models, at low redshifts ($z \leq 3$) the ratio of dust-to-stellar mass decreases with increasing stellar mass. At higher redshifts, the mass ratio is roughly independent of stellar mass. For each redshift interval, we fitted the following relationship to the data points for star-former:

$$\frac{M_*}{M_s} = a\log_{10}M_* + b \quad (5)$$

The fits are shown in the figure and Table 1 lists our estimates of a and b.

Fig. 6 shows the mean ratio of dust-to-stellar mass plotted against redshift for each interval of stellar mass. For all three temperature models, there is a steady increase of the mass ratio with redshift in all mass intervals except in the two lowest mass intervals for evolve.

Fig. 7 shows the weighted mean value of the five values for the dust-to-stellar mass ratio in each redshift interval plotted against redshift. We have calculated these weighted means separately for each temperature model and used the errors on dust-to-stellar mass ratios shown in Fig. 6. For all three temperature models, the mass ratio increases with redshift out to $z \sim 2.5$. For cold and star-former, the mass ratio continues to increase with redshift at $z > 2$, but is fairly constant above this redshift for evolve.

We have compared our results at low redshift with the dust-scaling relations derived for the Herschel Reference Survey (HRS; L. Cortese et al. 2012). These authors used a method that is sensitive to the cold dust in a galaxy, which should produce similar results to our cold and star-former temperature models, and also used the same value for the dust emissivity index as ours. They used a different mass-opacity coefficient, but we have made a correction to their relationships to account for this. In the panel for the lowest redshift interval in Fig. 5 we have shown their relationships between the ratio of dust-to-stellar mass and stellar mass for the HRS galaxies inside and outside the Virgo Cluster. Apart from our measurement for the stellar mass bin with $10.5 < \log_{10}M_* < 11.0$, the HRS relationships agree very well with ours. The HRS relationships show the same decrease of the mass ratio with stellar mass that we find at all redshifts at $z < 3.5$

In Fig. 7 we have compared our estimates of the mean ratio of dust-to-stellar mass with estimates for individual galaxies from three programmes. At $z > 6$, we have used estimates of the ratio of dust-to-stellar mass in H. S. B. Algera et al. (2026), which are based on ALMA continuum measurements of galaxies in the Reionization Era Bright Emission Line Survey (REBELS; R. J. Bouwens et al. 2022). These estimates were made on the assumption of a dust temperature of 45 K (H. S. B. Algera et al. 2026). We have scaled these estimates to the values they would have if they had been based on our star-former temperature model and our value of the mass-opacity coefficient. At slightly lower redshifts ($4.4 < z < 5.9$), we have used the ALMA continuum measurements of galaxies in the ALMA Large Program to Investigate [C II] at Early times (ALPINE, M. Béthermin et al. 2020; O. Le Fèvre et al. 2020). We have used these measurements (M. Béthermin et al. 2020) plus the redshifts (A. L. Faisst et al. 2020) to estimate dust masses using our value for the mass-opacity coefficient and the STAR-FORMER temperature model, calculating the ratio of dust-to-stellar mass using the stellar mass estimates in A. L. Faisst et al. (2020). In the redshift range $0 < z < 2$, we have used estimates of the ratio of dust-to-stellar mass for several samples of galaxies with high far-IR luminosities in A. Kirkpatrick et al. (2017), who used *Herschel* and *Spitzer* measurements to estimate the dust masses. We have converted these to the same value of the mass-opacity coefficient that we use in this paper.[4]

Fig. 7 shows that the estimates from REBELS of the dust-to-stellar mass ratio are mostly higher than our estimate for the mean value at $6 < z < 8$. The estimates from ALPINE at $4.4 < z < 5.9$ are mostly upper limits but the detections are spread roughly equally above and below our estimate of the mean value. The estimates of the dust-to-stellar mass ratio for the low-redshift ($0 < z < 2$) sample are consistently higher than our estimate of the mean value. This last difference is perhaps not surprising because these galaxies are from samples of galaxies with high far-IR luminosities and so there is likely to be a selection effect favouring high values of the dust-to-stellar mass ratio (S. A. Eales & M. G. Edmunds 1996). There is not the same strong bias operating at higher redshifts, but both REBELS and ALPINE were targeted at galaxies with star formation rates above a minimum value (R. Bouwens et al. 2020; O. Le Fèvre et al. 2020), so there may be some bias in these samples towards higher values of the dust-to-stellar mass ratio, compared to our estimates which are for the mean value for all galaxies within a certain range of stellar mass.

[4] A. Kirkpatrick et al. (2017) estimated their dust masses using the model in J. C. Weingartner & B. T. Draine (2001), in which the mass-opacity coefficient depends on wavelength in a complex way. We have used the approximation for this relationship given in L. Liang et al. (2019).

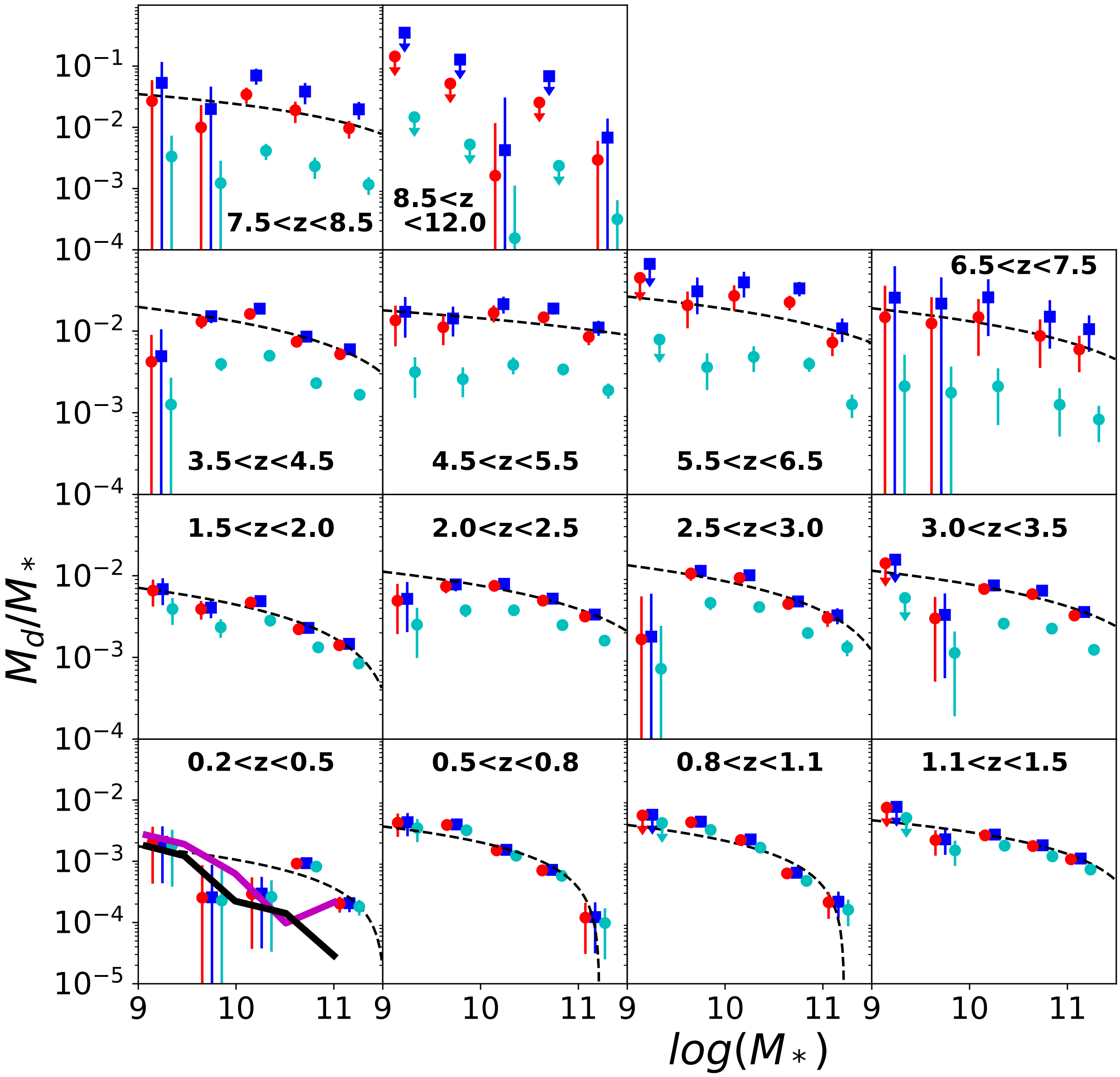

Figure 5. The mean ratio of dust-to-stellar mass versus stellar mass for the 14 redshift intervals. The coloured symbols show the results for the three temperature models: blue – cold; red – star-former; and cyan – evolve. The three sets of points have been offset by ± 0.1 along the x-axis for greater clarity. The upper limits are 3σ upper limits. The dashed lines show the result of fitting equation (5) to the data points for star-former. The two thick lines in the lowest redshift interval shows relationships derived for the Herschel Reference Survey (L. Cortese et al. 2012) after a correction has been made for the different value of the mass-opacity coefficient. The purple line is for galaxies outside the Virgo Cluster, the black line for galaxies inside the Virgo Cluster.

The main feature of Fig. 7 is the steady rise in the mean dust-to-stellar mass ratio with redshift. There is currently no submillimetre survey of a sufficiently large area of sky and with sufficient sensitivity to produce dust-mass estimates for a large percentage of the individual galaxies in a large unbiased sample in the redshift range $0 < z < 4$. However, studies like ours that use a statistical method to estimate the mean ratio do find an increase with redshift similar to the one we see (F. Calura et al. 2017; N. Scoville et al. 2017; J. S. Millard et al. 2020).

At the highest redshifts ($z > 8$), T. J. L. C. Bakx et al. (2026) estimated an upper limit for the mean ratio of dust-to-stellar mass. We have plotted their upper limit (for galaxies with $\log_{10} M_* > 9.0$) in Fig. 7, after making a correction for the different value of the mass-opacity coefficient, as the lower horizontal line in the figure. At first sight, this disagrees with our estimates in the redshift bin $7.5 < z < 8.5$. However, in estimating this limit, T. J. L. C. Bakx et al. (2026) assumed a dust temperature of 50 K. The upper horizontal line shows their upper limit if we recompute it using cold ($T = 22$ K). The dramatic difference shows the extreme sensitivity of dust-mass estimates at high redshift to the temperature model.

3.5 The evolution of the cosmic dust density

As in our previous paper (S. Eales & B. Ward 2024), we used the stacking measurements and the stellar mass function to calculate the mean density of dust in the universe in each redshift interval.

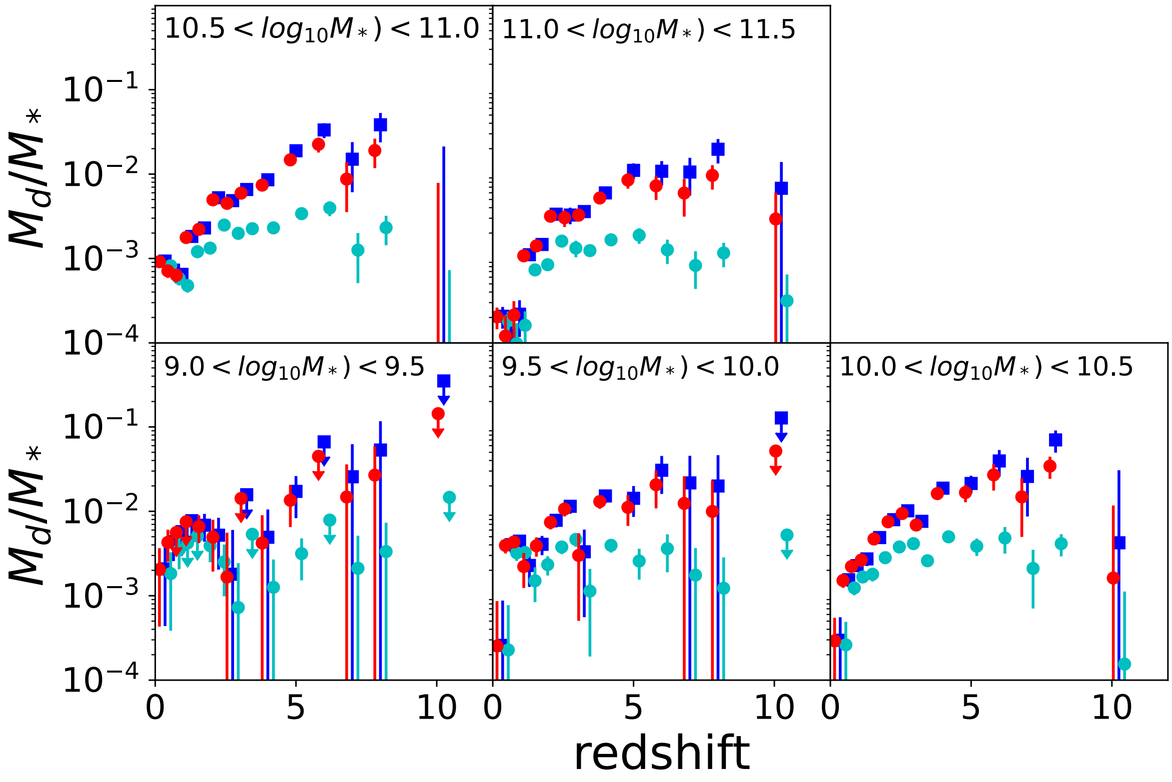

Figure 6. The mean ratio of dust-to-stellar mass versus redshift for the five intervals of stellar mass. The coloured symbols are for the different temperature models: blue – cold; red – star-former; and cyan – evolve. The sets of points have been offset by ±0.1 in redshift for greater clarity.

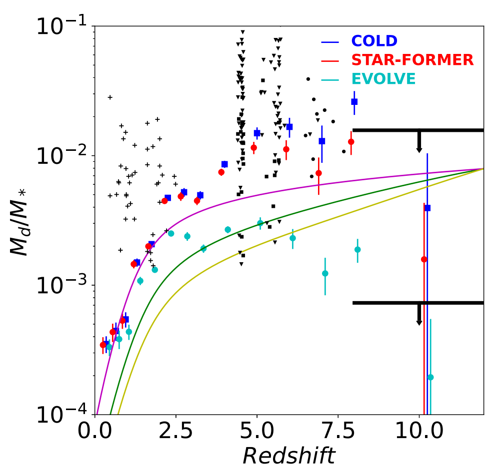

Figure 7. The mean ratio of dust-to-stellar mass (see the text for details) plotted against redshift. The coloured symbols are for the different temperature models: blue – cold; red – star-former; and cyan – evolve. The black symbols show estimates of the dust-to-stellar mass ratio for individual galaxies: crosses – A. Kirkpatrick et al. (2017); squares – M. Béthermin et al. (2020); and squares – H. S. B. Algera et al. (2026, see the text for more details). The lower horizontal line shows the upper limit for the mass ratio derived by T. J. L. C. Bakx et al. (2026) for galaxies at $z > 8$ and the upper limit shows our recalculation of this limit if we assume a dust temperature of 22 K. The three coloured lines are the predictions of our model for the evolution of the mass ratio (Section 4.5), with the purple line showing the prediction for a closed-box model ($\Lambda = 0$), the green line for a model with outflows and $\Lambda = 1$, and the yellow line for a model with outflows and $\Lambda = 2$.

We calculated the contribution to the dust density from the i'th sample, ρ_i, from the equation:

$$\rho_i = \frac{< \frac{M_d}{M_*} > \int_{z_L}^{z_U} \int_{M_L}^{M_U} \phi(M_*) M_* \mathrm{d}M_* \mathrm{d}V}{\int_{z_L}^{z_U} \mathrm{d}V} \quad (6)$$

in which M_* is the mass of stars in a galaxy and the integrals are over the mass and redshift limits for that sample. The mean ratio of dust-to-stellar mass that precedes the integral is our estimate for that sample (Section 3.4). We carried out the integration over the mass range $9.0 < \log_{10} M_* < 11.5$. We made no attempt to correct for the galaxies with masses outside this range because the corrections are so uncertain. In our previous paper (S. Eales et al. 2024), we did make an attempt to do this, finding corrections of $\simeq 10 - 20$ per cent to the mean dust density.

In applying equation (6), we used the tabulated values of the stellar mass function derived from the COSMOS-Web data (M. Shuntov et al. 2025b). The redshift ranges we have used for the samples (Table 1) are the same as those used to derive the COSMOS-Web stellar mass function, except that to maximize signal-to-noise ratio at high redshifts we combined the two highest redshift intervals used to derive the stellar mass function into a single-redshift interval. To derive the mean dust density in this redshift interval, we have therefore averaged the two COSMOS-Web stellar mass functions.

The mean density of dust in each redshift interval is then given by:

$$\rho = \sum_i \rho_i \quad (7)$$

in which the sum is over all the stellar-mass bins for that redshift interval.

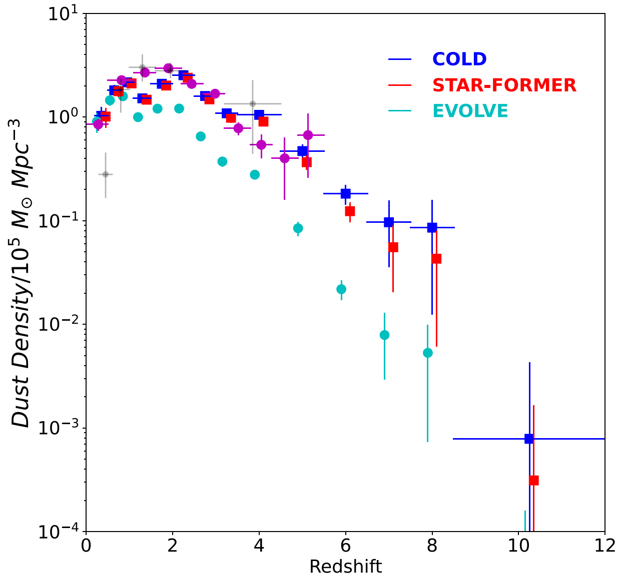

Figure 8. The mean dust density versus redshift for cold (blue), star-former (red), and evolve (cyan). The purple circles show our estimates based on the ground-based surveys of COSMOS (S. Eales & B. Ward 2024). The grey crosses show the estimates of B. Magnelli et al. (2020). A comparison of our results with other attempts to derive the relationship between mean dust density and redshift is given in our earlier paper (S. Eales & B. Ward 2024).

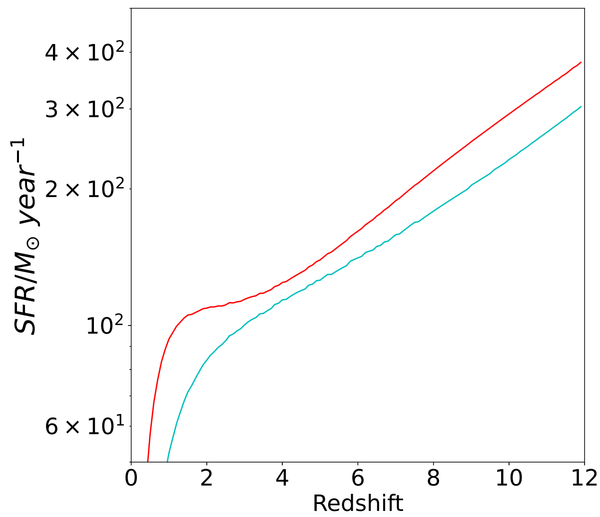

Figure 9. Estimated star formation rate versus redshift for a galaxy with an 850-μm flux density of 1 mJy (see the text for details) and for the temperature models: evolve (cyan) and star-former (red).

Fig. 8 shows the results. There is good agreement between the mean dust density derived with cold and star-former, which is not surprising because most of the dust in both models is cold. The estimates for evolve are lower, with the difference increasing with redshift. If the temperature estimates made from some of the stacking analyses turn out to be correct, the differences would be even larger. For example, if we used a temperature of 100 K for dust at $z \sim 7$ (M. P. Viero et al. 2022), our estimate of the global dust density at this redshift would be an additional factor of ~ 17 lower than the lowest of our three estimates.

The purple circles show the estimates from our earlier study, which used cold as the temperature model (S. Eales & B. Ward 2024). There is good overall agreement between our new estimates based on COSMOS-Web and our old estimates based on COSMOS. The significant differences at some redshifts (e.g. $1.1 < z < 1.5$) are mostly explained by differences in the stellar mass functions used in the two studies, which are probably the result of cosmic variance.

In our earlier paper (S. Eales & B. Ward 2024), we compared our estimates of the mean dust density with all other estimates we were aware of, and we refer the reader to that paper for a comparison of our results with other results. In the earlier paper, we overlooked one study (B. Magnelli et al. 2020), which was based on ALMA observations of the Hubble Ultra Deep Field. These estimates are shown in Fig. 8, which are consistent with ours although with much larger error bars.

4 DISCUSSION

4.1 The star formation rate estimated two ways

In this section, we switch our attention from dust masses to the bolometric dust luminosity. The reason for this is that in the context of galaxy evolution two of the most important properties of a galaxy are its star formation rate and its gas mass. Although the dust mass is often used to estimate the mass of gas in a galaxy (S. Eales et al. 2012; N. Scoville et al. 2016, 2017; L. J. Tacconi et al. 2020), the method depends on an assumption about the gas-to-dust ratio, which depends on the galaxy's metal abundance and which is a particular problem at high redshift where in general galaxies are likely to be less chemically evolved.

The bolometric dust luminosity, on the other hand, is one of the most direct ways of estimating the star formation rate in a galaxy (R. C. Kennicutt 1998; R. C. Kennicutt & N. J. Evans 2012). Newly formed OB massive stars spend a large portion of their lives hidden by dust and so a measurement of the bolometric dust emission provides a direct measurement of their energy output. In galaxies with low star formation rates, the estimate of the star formation rate from the bolometric dust emission may be too high because of the heating effect of the older stellar population (e.g. G. P. Ford et al. 2013), but in galaxies with high star formation rates – the most extreme examples being the SMGs – this is not likely to be a problem (R. C. Kennicutt 1998; R. C. Kennicutt & N. J. Evans 2012).

With a flux density measurement at only a single wavelength, we do need a model of the temperature of the dust. Fig. 9 shows the star formation rate plotted against redshift for a source with an 850-μm flux density of 1 mJy for star-former and evolve. We have not included cold because any galaxy containing OB stars must contain some warm dust. We estimated the star formation rate by integrating the SED of the dust model between wavelengths of 3 and 1100 μm to calculate the bolometric dust emission, then calculating the star formation rate using the calibration in R. C. Kennicutt & N. J. Evans (2012). This calibration was based on a Kroupa initial mass function, but a calibration based on a Chabrier initial mass function gives a very similar result (R. C. Kennicutt & N. J. Evans 2012).

The two temperature models give very similar results. We chose to use star-former to estimate the mean star formation rates for the COSMOS-Web galaxies for the reasons described in Section 2.7, but it would have made very little difference if we had used evolve.

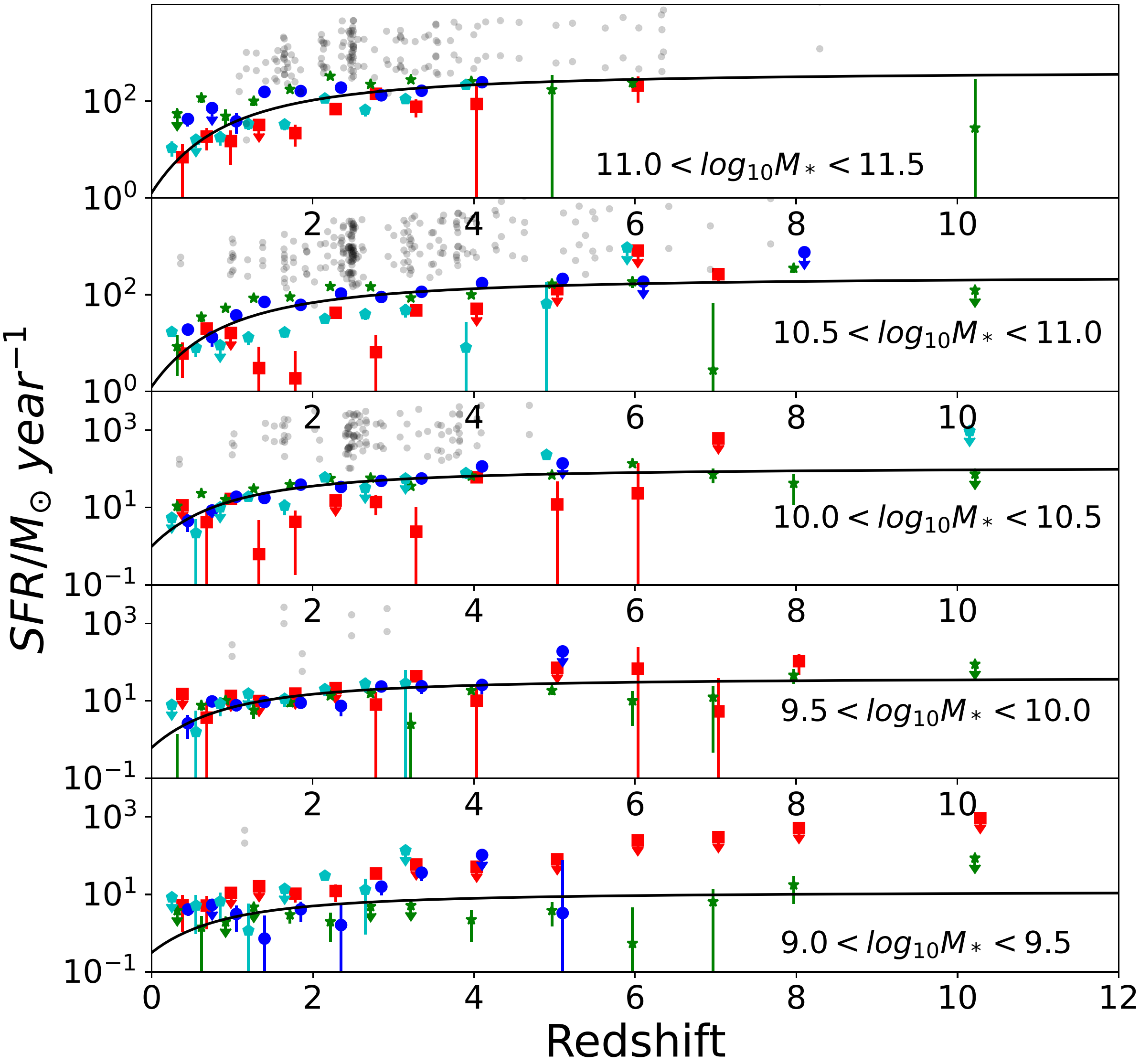

Figure 10. Mean value of the star formation rate estimated from the bolometric dust luminosity plotted against redshift, with the colour of the symbol showing the morphological class: red – spheroids; blue – disc-dominated galaxies; green – irregular galaxies; and cyan – bulge-dominated galaxies. The lines show the predicted relationships for the 'galaxy main sequence' (P. Popesso et al. 2023). The upper limits are 3σ upper limits. The grey points are the SMGs in COSMOS-Web (J. McKinney et al. 2025).

Fig. 10 shows the mean star formation rate plotted against redshift for the 280 samples, split into a separate panel for each mass interval. Many of the samples contain so many galaxies that the formal errors are very small, making the error bars invisible. The lines in the plot show the predicted relationships for the 'galaxy main sequence', using the relationships from P. Popesso et al. (2023, eq. 10 in that paper).

Fig. 10 shows that the mean star formation rate for all morphological classes increases with redshift, roughly following the prediction for the 'galaxy main sequence'. Even spheroidal galaxies, which today have very low star formation rates, had star formation rates that reached $\simeq 100$ M$_\odot$ yr^{-1} at $z > 2$. In our figure, the spheroids and bulge-dominated galaxies in the lowest redshift bin do have significant star formation rates, but since this bin covers the redshift range $0.2 < z < 0.5$, it is not really a local sample, and the *Herschel* ATLAS survey has shown there is strong evolution in the star formation rate and dust masses of galaxies over the redshift range $0 < z < 0.5$ (S. Dye et al. 2010; L. Dunne et al. 2011; S. Eales et al. 2018; R. A. Beeston et al. 2024).

Our conclusion that high-redshift spheroids have, on average, high star formation rates is not inconsistent with the claim that there is a large population of massive quiescent galaxies at high redshift (K. Glazebrook et al. 2017; P. Santini et al. 2021; A. C. Carnall et al. 2023a, b; T. Nanayakkara et al. 2024, 2025), since none of these studies separated galaxies by morphological type.

We have also included in the plot estimates of the star formation rate for the SMGs in COSMOS-Web. The term SMG was coined to refer to the galaxies discovered in the first submillimetre surveys, so it does not have a clear physical definition, but a practical definition comes from the flux limit of these original surveys: $\simeq$3 mJy (A. J. Barger et al. 1998; D. H. Hughes et al. 1998; S. Eales et al. 1999). We estimated the star formation rates for the SMGs in COSMOS-Web (J. McKinney et al. 2025) using the 850-μm flux densities of the individual SMGs and the same method as

Table 3. Morphological classification of COSMOS-Web SMGs.

Classification	No. of SMGs
Unclassified	39
Spheroids	6
Disc-dominated	63
Irregular	137
Bulge-dominated	22

for the stacked samples. Given the difference between our stacked signals and the detection limit for the original submillimetre surveys, it is not surprising that the SMGs have much higher star formation rates than our morphological samples.

We note the important point that this difference does not necessarily mean the SMGs are a physically distinct class of galaxies from the general population, since our star formation rates for the morphological classes are estimates of the mean star formation rate for each class, so the SMGs might simply be extreme members of a class rather than something unique. Table 3 shows the number of SMGs in COSMOS-Web that fall in the different morphological classes. There is a much higher fraction of irregular and disc-dominated galaxies than in the general population, although there are still significant numbers of spheroids and bulge-domimnated galaxies.

Fig. 11 shows the ratio of our estimate of the mean star formation rates to the mean of the COSMOS-Web estimates for the same galaxies, which were derived from fits of stellar synthesis models to their UV-to-near-IR SEDs (Section 2.2), plotted against redshift. We have also plotted this ratio for the SMGs. The figure shows that for the SMGs the estimate from the dust emission is often much higher than the estimate from the UV-to-near-IR SED, showing, as is well known, that the dust obscuration in these galaxies is often so high (J. M. Simpson et al. 2017; U. Dudzevičiūtė et al. 2020; K. C. Harrington et al. 2021) that attempts to estimate the star formation rate by fitting population synthesis models to the UV-to-near-IR SEDs fail catastrophically. On the other hand, for the COSMOS-Web galaxies in general there is no strong evidence for any systematic difference between the star formation rate estimated from the dust emission and one estimated from fitting a population synthesis model.

4.2 Is quenching already happening?

Analysis of the morphological classifications of the COSMOS-Web galaxies suggests that the familiar morphological types – the *Hubble* sequence – came into existence at $z \sim 4$ (M. Huertas-Company et al. 2025). In the universe today, there is a clear progression along the *Hubble* sequence from the irregulars and disc-dominated systems, which are generally gas-rich and with high star formation rates, to the bulge-dominated and spheroidal galaxies at the other end of the sequence, which contain less gas and have lower star formation rates (R. C. Kennicutt 1998; A. Saintonge & B. Catinella 2022). There must therefore be some quenching process that has differentially reduced the star formation rate along the *Hubble* sequence. An obvious question to ask is: when did this differential quenching process start?

There is already some indication in Fig. 10 that at high redshifts and high stellar masses the mean star formation rate for the spheroids and the bulge-dominated galaxies is lower than for the other two morphological classes. In this section, we try to quantify this difference. We focus on the redshift range $2 < z < 4.5$, which is roughly where analysis of the spectra of low-redshift massive ellipticals implies most of the stars in these galaxies must have formed (D. Thomas et al. 2005, 2010). We only consider galaxies with $\log_{10}M_* > 10.0$ because most galaxies with lower stellar masses are irregulars.

Fig. 12 shows the mean star formation rate for the galaxies in this redshift range for the four morphological classes, arranged in order along the *Hubble* sequence. The figure shows that for each of the three mass intervals there is a clear progression along the *Hubble* sequence with the mean star formation rate increasing by a factor of $\simeq 4$ from spheroids to irregulars.

Fig. 13 shows a similar analysis for this redshift range using the star formation rate estimates from the UV-to-near-IR SEDs in the COSMOS-Web catalogue. In this case, we have plotted histograms of the specific star formation rate (star formation rate divided by stellar mass – SSFR) for the four morphological classes, only including galaxies with $\log_{10}M_* > 10.5$ because otherwise the histograms become dominated by the galaxies in the lowest of the three mass bins shown in Fig. 12. This figure shows the same things as Fig. 12. There is a steady increase in this redshift range in the median values of SSFR along the *Hubble* sequence.

Both figures imply that even in an epoch that was only shortly after the *Hubble* sequence came into existence, differential quenching was already in progress. This conclusion does not depend on the accuracy of the morphological classifications because any classification errors will tend to reduce any differences observed between the classes.

We have also plotted in the spheroid panel a histogram of the values of SSFR for the ellipticals in the Herschel Reference Survey, a volume-limited survey of the nearby universe (A. Boselli et al. 2010; S. Eales et al. 2017). The difference in SSFR between these low-redshift galaxies and most of the spheroids in COSMOS-Web shows that even if quenching was already in action, it had a long way to go.

4.3 When did quenching start and how fast did it happen?

Answers to both these questions are suggested by the form of the histograms in Fig. 13. The histograms of SSFR for both the irregulars and the disc-dominated galaxies have clear peaks in this figure, which is similar to the expected values for the 'galaxy main sequence' (P. Popesso et al. 2023). It seems a reasonable assumption that this would be where galaxies would be in the absence of any quenching process. The histogram for the spheroids shows no peak at all at this value of SSFR, suggesting that quenching must have started either immediately after or even before the formation of the structures of the spheroids. The histogram for the bulge-dominated galaxies shows a slight peak and then a long tail to lower values of SSFR, suggesting that quenching started some time after the formation of the galaxy's structure.

The form of the spheroid histogram also suggest that the quenching process is not very fast. Suppose, for example, the quenching occurs as the result of the formation of a quasar at the centre of the galaxy some time after the formation of its spheroidal structure, with the gas then driven out by the pressure of the radiation from the quasar (A. C. Fabian 2012; F. Bollati et al. 2024), rapidly shutting off star formation. In this case, we would expect to see a histogram with two peaks rather than the flat histogram we actually observe.

We have estimated a time-scale for the quenching of the star formation in the spheroidal class using the following very simple model. We make the assumption that the moment the structure

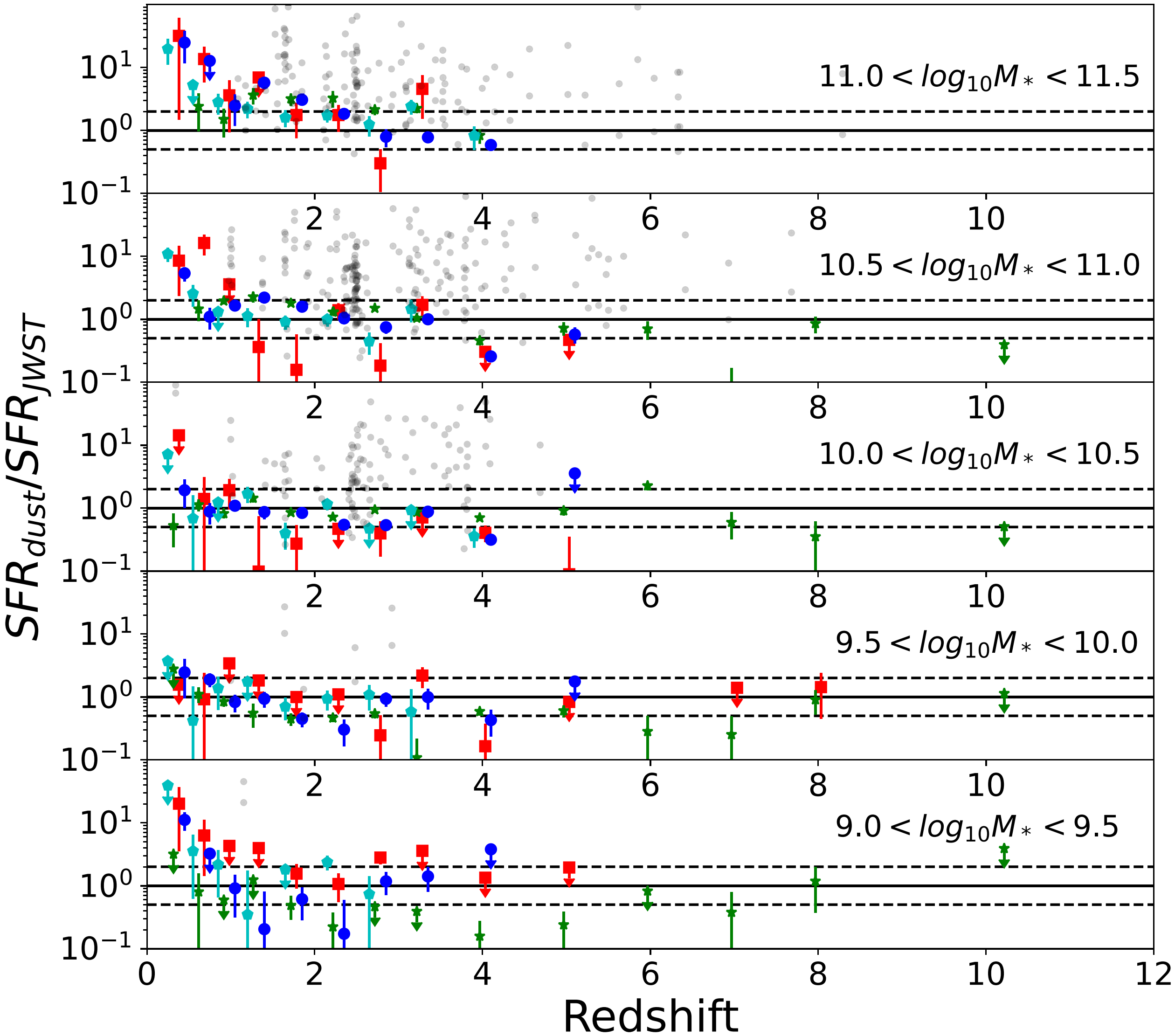

Figure 11. Ratio of the mean star formation rate estimate from the dust emission to the mean of the COSMOS-Web estimates from the UV-to-near-IR SED for the same sample of galaxies. The continuous horizontal line shows where the two estimates are equal and the two dashed lines show where the star formation rate estimated from the dust emission is 2 or 0.5 times the COSMOS-Web estimate. The colours show the different morphological types: red – spheroidal galaxies; blue – disc-dominated galaxies; green – irregular galaxies; and cyan – bulge-dominated galaxies. The upper limits are 3σ upper limits. The grey points are SMGs in COSMOS-Web (J. McKinney et al. 2025).

of the spheroid is formed the quenching process starts. We assume that the spheroid initially has a specific star formation rate ($SSFR_{init}$) that puts it on the galaxy 'main sequence' (P. Popesso et al. 2023). We make the additional assumption, which is suggested by the flat histogram, that the quenching occurs by some kind of 'starvation' process in which the gas supply is shut-off and the star formation rate then falls as the result of the gradual depletion of the galaxy's gas reservoir by the formation of new stars. With this assumption, the star formation rate, SFR(t), then depends on time in the following way:

$$SFR(t) = SFR_{init} \times \exp(-t/\tau_{dep})$$

in which SFR_{init} is the initial star formation rate, t is the time since the gas supply was shut-off, and τ_{dep} is the depletion time, the one adjustable parameter in our very simple model. We make the simplifying assumption that the stellar mass of the galaxy does not change significantly after the quenching starts, so we can also write:

$$SSFR(t) = SSFR_{init} \times \exp(-t/\tau_{dep})$$

Our final assumptions are that massive spheroids are produced at a constant rate over the redshift range $2 < z < 4.4$ and that $SSFR_{init}$ remains constant, with a value of −8.9, over this redshift range. We can safely assume that as the star formation rate in the galaxy falls, it will still remain above the COSMOS-Web detection limit since the galaxies in Fig. 13 are well above the COSMOS-Web stellar mass limit (M. Shuntov et al. 2025a).

The lines in Fig. 13 shows the predictions of the model for three different depletion times. The model that provides the best fit to the histogram has a depletion time of $\tau_{dep} = 10^{8.2}$ yr. Shorter depletion times produce too many galaxies with low values of SSFR and vice versa. This is a shorter depletion time than that found for low-redshift starbursts ($\tau_{dep} \simeq 10^{8.5}$ yr; R. C. Kennicutt & M.

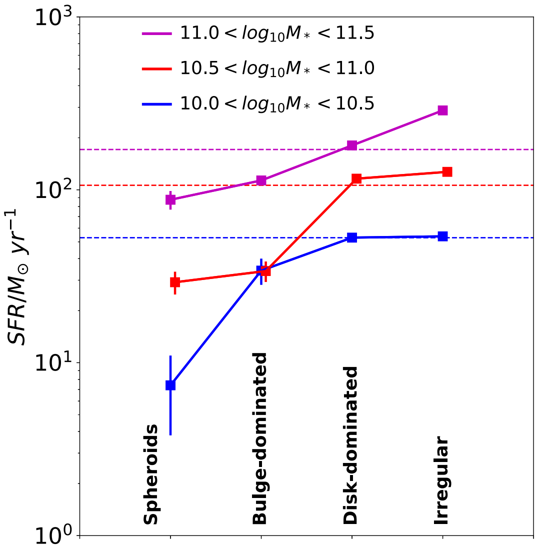

Figure 12. Mean star formation rate estimated from the dust emission for galaxies in the four morphological classs in the redshift range $2 < z < 4.5$ and $10.0 < \log_{10}M_* < 10.5$ (blue), $10.5 < \log_{10}M_* < 11.0$ (red), and $11.0 < \log_{10}M_* < 11.5$ (mauve). The horizontal dashed lines show the predicted star formation rate for a galaxy on the galaxy 'main sequence' at a redshift of 3 with $\log_{10}M_* = 10.25$ (blue), 10.5 (red), and 11.25 (mauve).

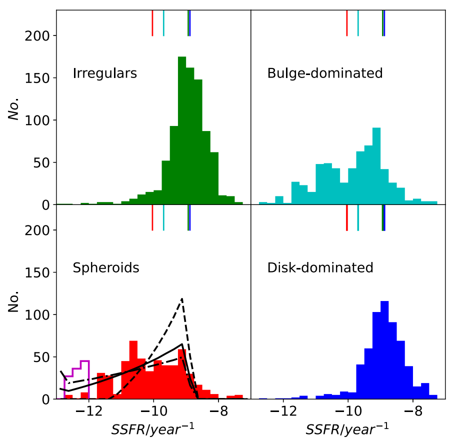

Figure 13. Histograms of the specific star formation rate for the four morphological classes in the redshift range $2 < z < 4.5$ and with $11.5 > \log_{10}M_* > 10.5$. In this case, the star formation rates are the values estimated from UV-to-near-IR photometry in the COSMOS-Web catalogue (Section 2.2). The vertical lines show the median values of SSFR for the four classes. The lines for the irregulars and the disc-dominated are so close as to be indistinguishable. The lines in the spheroid panel shows the prediction of the quenching model described in Section 4.3 for gas depletion times of 10^8 yr (dot–dashed), $10^{8.2}$ yr (solid), and $10^{8.5}$ yr (dashed). The unfilled histogram in the spheroid panel show the distribution of SSFR for the elliptical galaxies in the Herschel Reference Survey (P. De Vis et al. 2017).

A. C. De Los Reyes 2021), but longer than the typical depletion time for SMGs (S. Dye et al. 2015, 2022).

4.4 Do massive spheroidal and bulge-dominated galaxies pass through an SMG phase?

In Section 4.1, we noted that the SMGs are not necessarily a distinct population from other disc-dominated and irregular

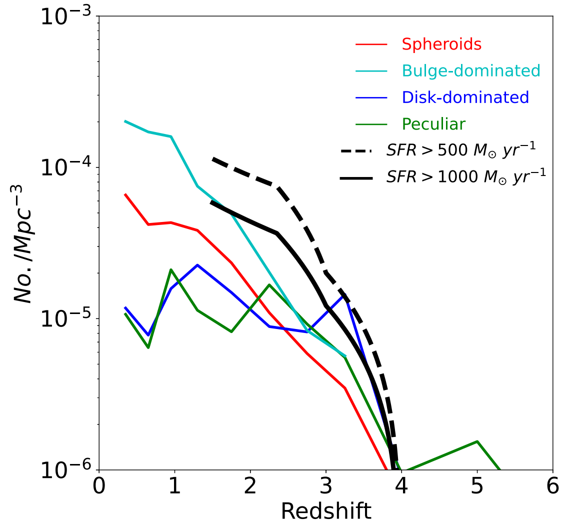

Figure 14. The space density of galaxies in the mass range $11.0 < \log_{10}M_* < 11.5$ with irregular morphologies (green), disc-dominated morphologies (blue), bulge-dominated morphologies (cyan), and spheroidal morphologies (red), calculated from the COSMOS-Web stellar mass function (M. Huertas-Company et al. 2025). The solid and dashed blacks lines shows the predictions of the model for the production of bulge-dominated and spehroidal galaxies from SMGs in the same range of stellar mass for a lower star formation limit of 500 and 1000 $M_\odot$ yr^{-1}, respectively.

galaxies, but might simply be extreme members of this population with the highest star formation rates. Nevertheless, there is evidence that massive elliptical galaxies did pass through an early phase in which their star formation rates were as high as those for the SMGs (D. Thomas et al. 2005, 2010). Therefore, even if the SMGs are not a separate population, it is still valid to ask whether there are enough SMGs for them to represent this early phase in the lives of massive early-type galaxies.

Previous studies have shown that there are enough SMGs for them to be the ancestral population of massive quiescent galaxies at $z > 1$ (F. Valentino et al. 2020; A. S. Long et al. 2023). These studies, however, did not have access to the *JWST* morphological classifications. In this section, we construct a model to test whether the rate of growth in the number density of massive spheroidal and bulge-dominated galaxies as found in COSMOS-Web is what one would expect from the properties of the SMG population.

Fig. 14 shows the space density of galaxies with stellar masses in the range $11.0 < \log_{10}M_* < 11.5$ plotted against redshift for the four different morphological classes, which we have calculated from the stellar mass functions for these classes (M. Huertas-Company et al. 2025). The figure shows that the relationship is steeper for the spheroidal and bulge-dominated galaxies than for the irregulars and disc-dominated galaxies. (This figure is also prima-facie evidence that massive disc-dominated and irregular galaxies must be morphologically transformed into something else because otherwise the relationships for these morphological types would be steeper than horizontal because of the continual formation of new stars out of gas within existing galaxies.)

Our model is based on the assumption that SMGs reach stellar masses of $\log_{10}M_* > 11.0$ before the star formation is quenched. This seems a reasonable assumption since a large fraction of SMGs already have stellar masses above this value (J. M. Simpson et al. 2017; S. Eales et al. 2024). We start with the estimates of the space density of SMGs as a function of bolometric luminosity, $\phi(L_{\rm bol})$, estimated by U. Dudzevičiūtė et al. (2020) for the redshift ranges $z < 2.35$, $2.35 < z < 3.0$, and $z > 3.0$. For any galaxy we can estimate the value of its star formation rate from its bolometric luminosity using the calibration given in R. C. Kennicutt & N. J. Evans (2012), which allows us to convert the space density of SMGs as a function of bolometric luminosity into the space density of SMGs as a function of star formation rate.

The time required for an SMG to reach a stellar mass of 10^{11} M$_\odot$ is given by:

$$\tau_{\rm lifetime} = \frac{10^{11}}{\rm SFR}\ {\rm yr}$$

in which SFR is its star formation rate. The number of galaxies with stellar masses above this mass ($N > 10^{11}$ M$_\odot$) generated by the SMG population is given by:

$$N(t) = \int_{t_{\rm start}}^{t} \int_{{\rm SFR}_{\rm min}(L_{\rm bol})}^{\infty} \frac{\phi(L_{\rm bol})}{\tau_{\rm lifetime}} {\rm d}L_{\rm bol}{\rm d}t$$

in which $t_{\rm start}$ is the cosmic time at which the SMG epoch started. We used this equation to predict the increase in the number of massive galaxies over the redshift range $1.5 < z < 4$, the redshift range in which SMGs are mostly found, using the luminosity functions mentioned above for two different lower limits for the star formation rate: 500 and 1000 M$_\odot$ yr^{-1}.

Fig. 14 shows the results. The predictions for the model are very similar to the COSMOS-Web results for the growth in the number density of massive spheroidal and bulge-dominated galaxies.

The figure shows that the growth in the number density of massive spheroidal and bulge-dominated galaxies is roughly what one would expect if all these galaxies pass through an SMG phase. The space density of massive spheroidal and bulge-dominated galaxies continues to climb at lower redshifts, which our model does not explain because of the lack of SMGs at lower redshifts. The production of massive early-types galaxies, spheroids, and bulge-dominated galaxies, is therefore not solely the result of the conversion of this seed population.

4.5 The evolution of dust in the universe

In this section, we try to understand the evolution in the mean dust density in the universe shown in Fig. 8. We will also try to understand why the ratio of dust-to-stellar mass increases with redshift (Fig. 7).

There are now a very large number of sophisticated models for the evolution of dust in galaxies (e.g. H. L. Morgan & M. G. Edmunds 2003; R. S. Asano et al. 2013; S. Zhukovska et al. 2016; R. McKinnon et al. 2017; G. Popping, R. S. Somerville & M. Galametz 2017; S. Aoyama et al. 2018; A. P. Vijayan et al. 2019). These all attempt to incorporate in different ways the complex physics of how dust is formed in stars and then distributed into the ISM (interstellar medium). B. Magnelli et al. (2020), who found a similar relationship between mean dust density and redshift to ours (Fig. 8), tested some of these models, finding that they were not able to reproduce the observed relationship (G. Popping et al. 2017; S. Aoyama et al. 2018; Q. Li, D. Narayanan & R. Davé 2019; A. P. Vijayan et al. 2019).

In this section, we make a zeroth-order attempt to understand the relationships in Figs 7 and 8 by using a simple model that cuts out all the complex, and uncertain, physics. In our earlier paper (S. Eales & B. Ward 2024), we pointed out the similarity of the star formation history of the universe and the relationship between the mean dust density and redshift, which was also noticed by B. Magnelli et al. (2020), with the only difference being that at $z > 2$ the mean dust density falls more rapidly with redshift than the mean star formation rate. One of the advantages of our modelling approach is that, by stripping away the complexity, it makes it possible to get an understanding of the relationship between the star formation history and the evolution of the dust.

The first assumption of the model is that a constant fraction of the metals in the ISM in a galaxy are incorporated in dust grains. There is evidence, from observations of galaxies in the Local Group and damped Lyman alpha systems, that this is true for galaxies with high metal abundances, with about half the metals being incorporated in dust (A. De Cia et al. 2016; J. Roman-Duval et al. 2022a, b). The slope of the relationship between the dust-to-gas ratio and metal abundance is less than one (J. Roman-Duval et al. 2022b), so the fraction of the metals incorporated in the dust grains will be lower in galaxies with low metal abundance, but in this initial simple model we assume it is a constant. The advantage of this assumption is that we can avoid the poorly understood physics of how the metals are incorporated in the dust (S. Zhukovska et al. 2016) and use standard chemical evolution models to model the evolution of the dust.

The chemical evolution model we use is a simple analytic model, which relates the evolution of the mean metal abundance in a galaxy to the star formation rate, the inflow of gas and the outflow of gas. We refer the reader to M. G. Edmunds (1990) for a full description of the model, but we give here its main points.

The model is based on three additional assumptions. The first is that the mixing of metals within a galaxy is instantaneous, so the chemical evolution of the galaxy can be fully represented by the evolution in the mean metal abundance. The second is that the yield – the mass of metals produced by 1 solar mass of newly formed stars – is a constant. The third is the assumption of 'instantaneous recycling', in which the metals that will eventually be produced by a generation of stars are, in the model, deposited in the ISM the moment the stars are born. This assumption becomes dubious at very high redshifts when the ages of stars are similar to the age of the universe (S. Eales et al. 2024), but it is a powerful assumption because it makes it possible to relate the metallicity at any time (and the amount of dust) to the star formation rate at the same time.

In the following equations, g is the mass of gas in a galaxy, s is the mass of stars in the galaxy, R is the fraction of the mass of a generation of stars that is ultimately returned to the ISM rather than being locked up in stellar remnants and very long-lived stars, y is the yield, the mass of metals produced by one solar mass of newly formed stars, and Z is the metal abundance of the gas. We assume that the outflow of gas from the galaxy is given by Λ times the star formation rate and the inflow of gas (assumed to contain no metals) is allowed to have an arbitrary dependence on time given by $\Phi(t)$.

The two basic equations from the chemical evolution model (M. G. Edmunds 1990) are as follows. The change in the mass of metals in the gas is given by:

$$ {\rm d}(Zg) = Ry{\rm d}s - (1 - R)Z{\rm d}s - \Lambda Z{\rm d}s \quad (8)$$

In this equation, the first term on the right-hand side is the mass of metals injected into the ISM by newly formed stars. The second term is the mass of metals locked up in stellar remnants and long-lived stars. The third term is the mass of metals ejected from the galaxy. The change in the mass of gas in the galaxy is given by:

$$\mathrm{d}g = \Phi \mathrm{d}t - (1 - R)\mathrm{d}s - \Lambda \mathrm{d}s \quad (9)$$

We can now manipulate these equations into a form that is useful for a model for the evolution of the dust. Re-organizing the second equation a little gives:

$$\Phi(t) = \frac{\mathrm{d}g}{\mathrm{d}t} + \Lambda\frac{\mathrm{d}s}{\mathrm{d}t} + (1 - R)\frac{\mathrm{d}s}{\mathrm{d}t} \quad (10)$$

Combining the two equations yields:

$$\frac{\mathrm{d}Z}{\mathrm{d}t} = \frac{Ry}{g}\frac{\mathrm{d}s}{\mathrm{d}t} - \frac{Z\Phi}{g} \quad (11)$$

We can also write down a third equation if we assume that the star formation rate in a galaxy is proportional to the mass of gas it contains (R. C. Kennicutt 1998; R. C. Kennicutt & N. J. Evans 2012):

$$\frac{\mathrm{d}s}{\mathrm{d}t} = \frac{g}{\tau_{\mathrm{dep}}} \quad (12)$$

in which τ_{dep} is the depletion time of the gas in the galaxy.

This simple model of the evolution of the metal abundance in a galaxy can be simply adapted to model the mass of dust in a galaxy with the assumption that the mass of dust is given by:

$$M_d = \epsilon_d Z g \quad (13)$$

in which ϵ_d is the fraction of the metals locked up in dust grains.

This simple model has been used before to model the evolution of the dust in individual galaxies (S. A. Eales & M. G. Edmunds 1996, 1997; M. G. Edmunds & S. A. Eales 1998). In this paper, we extend it to the universe as a whole. The necessary assumptions are virtually the same. In the case of an individual galaxy, although though there are radial metallicity gradients in galaxies (R. Maiolino & F. Mannucci 2019), it is necessary to assume that the chemical evolution of a galaxy can be fully described by the evolution of the mean metal abundance. In the case of the universe, one has to make effectively the same assumption – that although the metal abundances of the galaxies in a volume of space are certainly very different, the chemical evolution of the universe can be usefully modelled by the change in its mean metal abundance. In this extension of the model to the universe as a whole, g is now the mean density of gas in the universe, s is the mean stellar density, Φ is the mean flow of pristine gas into galaxies, $\Lambda\frac{\mathrm{d}s}{\mathrm{d}t}$ is the mean outflow of gas from galaxies into the intergalactic medium, and M_d is the mean density of dust.

We implemented the model in the following way. We used the analytic expression for the star formation history of the universe (P. Madau & M. Dickinson 2014) and equation (12) to deduce the relationship between the mean gas density and redshift, using a depletion time of $10^{8.5}$ yr, a value appropriate for galaxies with high star formation rates (R. C. Kennicutt & M. A. C. De Los Reyes 2021). Many authors have argued that the depletion time varies with redshift (N. Scoville et al. 2016, 2017; L. J. Tacconi et al. 2020; N. Scoville et al. 2023), so our assumption of a constant value could be wrong, but it is useful simplification, and we also argue in the next section that the evidence for a changing depletion time may be at least partly caused by changes in the gas-to-dust ratio.

With the star formation history and the relationship between gas density and redshift, we are then able to use equation (10) to calculate the time dependence of the rate of inflow of pristine gas, $\Phi(t)$. We then integrate equation (11) to derive the evolution of the mean metal abundance of the universe, starting with $Z = 0$ at $t = 0$, and then use equation (13) to derive the evolution of the mean dust density. In our model, we use a value for ϵ_d of 0.52 (J. Roman-Duval et al. 2022b), and values for R and y of 0.38 and 0.04, respectively, which are appropriate for a Chabrier initial mass function (S. Eales et al. 2024).

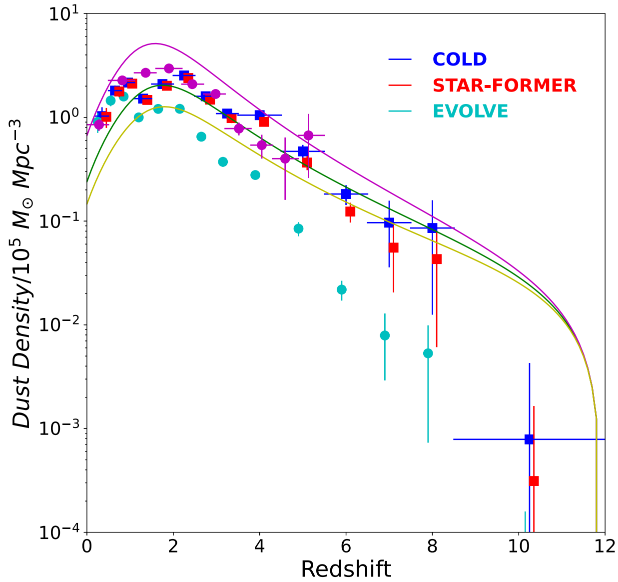

Figure 15. The same as Fig. 8 with the addition of the predictions of our model for the evolution of cosmic dust (see the text). The purple line is for a closed-box model, the green line for an outflow model with $\Lambda = 1$, and the yellow line for an outflow model with $\Lambda = 2$.

Fig. 15 shows the results for $\Lambda = 0$, 1, and 2. The model agree well with the mean dust density calculated with cold and star-former but predicts more dust in the early universe than the estimates for evolve. Of the three dust-evolution models, the one that agrees best with the data (as calculated with the first two temperature models) is the model with outflow parameter $\Lambda = 1$.

We can extend this model to make a prediction for how the ratio of dust-to-stellar mass should change with redshift. We calculated the relationship between the mean stellar density and redshift by integrating the analytic expression for the star formation history (P. Madau & M. Dickinson 2014). It is then a simple matter to calculate how the ratio of the dust-to-stellar mass should depend on redshift from the relationship between mean dust density and redshift calculated above. The predictions for the three dust-evolution models are shown in Fig. 7. In this case, the agreement between the model predictions and the observations is not so compelling, but the observed increase in the mass ratio with redshift is clearly seen in all three models.

This simple model allows an intuitive understanding of why the ratio of the mass of dust to stars is greatest at early times. Equation (8) shows that the change in the mean metal density (and in our model the mean dust density) is comprised of three components. One of these, the formation of metals in stars, leads to an increase in the mean metal density. The two others – outflows and the consumption of metals when new stars are formed (astration) – lead to a reduction in the mean metal density. The two latter terms are proportional to the metal abundance in the gas.

Since we assume that the metal production is proportional to the star formation rate, the mass of metals (and dust) in the ISM and the mass of stars will initially increase at the same rate when there are no metals in the ISM. But as the metals build up in the ISM and depletion from outflows and astration become significant, the mass of metals and dust in the ISM will increase at a slower rate than the mass of stars. Therefore, it is not surprising that the model predicts that the ratio of the mass of dust to the mass of stars should be greatest at early times when not much dust production has occurred. We note the caveat that this is also when the limitations of our simple model will be most apparent, since we have made the useful simplifying assumption that the dust is instantly made when the stars are formed and this will be a poor approximation when the age of the universe is similar to the lifetimes of stars.

4.6 The evolution of dust-traced gas in the universe

Dust has some major advantages over CO for estimating the amount of molecular gas in a galaxy (S. Eales et al. 2012; G. E. Magdis et al. 2012; N. Scoville et al. 2014; L. J. Tacconi et al. 2020; L. Dunne et al. 2022). In this section, we use the estimates of the cosmic dust density (Section 3.5) to estimate how the mean density of dust-traced gas changes with redshift.

We assume, fairly arbitrarily, that the average gas-to-dust ratio in galaxies today is 100. Many recent *JWST* studies have shown that the typical metal abundance in galaxies decreaes with increasing redshift (R. S. Ellis 2025, and references therein). There is now a reasonably consistent picture that the metal abundance in galaxies falls by 0.8 dex from $z = 0$ to 3, with a smaller decline of 0.2 dex from $z = 3$ to 10 (R. S. Ellis 2025). We assume the following relationships between metal abundance, A, and redshift that are consistent with these conclusions:

$$\log_{10}A = \log_{10}A(z = 0) - 0.267z \quad 0 < z < 3 \qquad (14)$$

$$\log_{10}A = \log_{10}A(z = 0) - 0.714 - 0.0286z \quad 3 < z < 10 \qquad (15)$$

Although the metal abundance also depends on the mass of the galaxy (R. Maiolino & F. Mannucci 2019), we have not got any straightforward way of including the mass dependence in our anyalysis, and anyway the mass dependence is poorly known at the highest redshifts. Therefore, in this initial attempt to make a correction for the evolution in the gas-to-dust ratio, we have not included any dependence on stellar mass.

On the assumption that the dust-to-gas ratio is proportional to the metal abundance (A. De Cia et al. 2016; J. Roman-Duval et al. 2022b), we used these relationships to calculate how the dust-to-gas ratio changes with redshift. With these relationships, the gas-to-dust ratio increases from 100 at $z = 0$ to $\simeq$720 at $z = 5$ and $\simeq$1000 at $z = 10$.

We use this relationship between gas-to-dust ratio and redshift to calculate the gas density from the estimates of the mean dust density for the three temperature models (Section 2.7). Fig. 16 shows the result. The dashed line and the coloured band show a recent estimate and its uncertainty for the evolution of the CO-traced gas (C. Péroux & J. C. Howk 2020). The shape of the two relationships, one for CO-traced gas and one for dust-traced gas, are very similar. There is a vertical offset, but this is not surprising given our fairly arbitrary choice of gas-to-dust ratio and that our estimate also depends on our choice of dust-mass-opacity coefficient. There is a similar uncertainty in the scaling of the relationship for CO because of the uncertainty in the CO calibration factor (A. D. Bolatto, M. Wolfire & A. K. Leroy 2013; L. Dunne et al. 2022).[5]

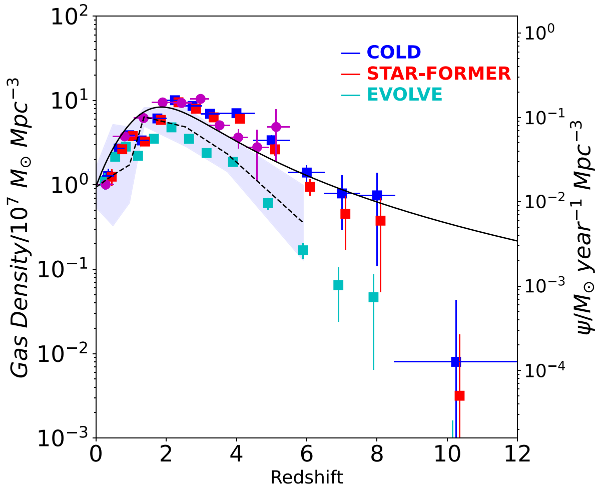

Figure 16. The mean density of dust-traced gas versus redshift for cold (blue), star-former (red), and evolve (cyan) and from our previous study (purple). The solid line shows the 'star formation history of the universe', an analytic relationship derived from empirical estimates of the global star formation rate (P. Madau & M. Dickinson 2014). The star-formation-density axis has been scaled so that the star formation history coincides with our measurements of the gas density, with the scaling corresponding to a gas depletion time of 6.3×10^8 yr. The dashed line and the coloured band show the best current estimates and their uncertainty for the CO-traced gas (C. Péroux & J. C. Howk 2020).

We have overplotted a relationship derived for the star formation history of the universe (P. Madau & M. Dickinson 2014). We have scaled the two vertical axes so that our relationship between dust-traced gas and the star formation history coincide as far as is possible. The scaling corresponds to a gas depletion time of:

$$\tau_{\rm dep} = 6.3 \times 10^8 \left(\frac{\rm gtd}{100}\right) \ {\rm yr}$$

in which gtd is the gas-to-dust ratio. With our fairly arbitrary assumption that the gas-to-dust ratio is 100, our estimate of the gas depletion time is similar to the values found by L. J. Tacconi et al. (2020) at $z \simeq 1$.

Although the scaling has been chosen in this way, the forms of the star formation history and the relationship between dust-traced gas and redshift are remarkably similar. This is only true, though, for cold and star-former. The similarity of the relationships, at least with our preferred star-former temperature model, is quite remarkable. It suggests that the gas depletion time, or conversely the star formation efficiency, is independent of redshift. This conclusion does differ from claims in the literature that the depletion time decreases with redshift (N. Scoville et al. 2016, 2017, 2023; L. J. Tacconi et al. 2020). The difference arises because we have assumed that the gas-to-dust ratio increases with redshift whereas Scoville and collaborators, whose work is most easily comparable to ours, assume that the gas-to-dust ratio is a constant.

[5]In our previous paper (S. Eales & B. Ward 2024), we used a slightly different method so that the calibrations of the dust and the CO were self-consistent. We still ended up with a vertical offset.

5 CONCLUSIONS

We have used two different stacking techniques to measure the mean submillimetre (850 μm) flux density for galaxies in the COSMOS-Web catalogue separated into samples by stellar mass, redshift and morphological class. The two techniques gives similar results, showing a gradual increase of submillimetre flux density with redshift, and at each redshift a positive correlation between flux density and stellar mass.

We converted the submillimetre flux densities into dust masses and bolometric dust luminosities using three different temperature models. We have tried to avoid the temperature bias that arises from fitting a single modified blackbody to a galaxy SED by using a more sophisticated model based on the SEDs of real star-forming galaxies. We have included the two other models to show the effect on our results of the range of dust temperatures in the literature. We have used our stacking results and temperature models to obtain the following results:

(i) We have used our stacking results and temperature models to determine the mean bolometric dust luminosities for each sample and thus estimate the mean star formation rate for each sample. In contrast to the situation for SMGs, we find no evidence for any systematic difference between our estimates of the star formation rate and the mean of the estimates in the COSMOS-Web catalogue, which were estimated from fitting stellar population synthesis models to the UV-to-near-IR SEDs.

(ii) The mean star formation rates for all morphological classes increase with redshift roughly following the relationship found for the 'galaxy main sequence' (P. Popesso et al. 2023), reaching star formation rates for the most massive galaxies ($M_* \sim 10^{11}$ M$_\odot$) of $\gtrsim 80$ M$_\odot$ yr^{-1} at $z > 2$.

(iii) In the redshift range $2 < z < 4.5$, the mean star formation rate decreases along the *Hubble* sequence from $\simeq 280$ M$_\odot$ yr^{-1} for irregular galaxies at one end to $\simeq 80$ M$_\odot$ yr^{-1}for spheroids at the other end. Since this is only shortly after the emergence of the *Hubble* sequence ($z \sim 4$; M. Huertas-Company et al. 2025), we conclude that quenching was already underway, or even before, the structures of the galaxies were formed.

(iv) We show that star formation rates for the high-redshift spheroids can be reproduced by a 'starvation' quenching model with a depletion time of $\simeq 10^{8.2}$ yr.

(v) We use the COSMOS-Web stellar mass functions (M. Huertas-Company et al. 2025) to investigate the growth of massive ($> 10^{11}$ M$_\odot$) galaxies of different morphological types over the redshift range $0 < z < 4$. The number density of massive irregular and disc-dominated galaxies is fairly constant while the number density of bulge-dominated and spheroidal galaxies increases steadily over this period. We construct a model based on the assumption that the seed population of massive spheroidal and bulge-dominated galaxies are 'SMGs' and show that this model can reproduce the growth in the number density of these galaxies over the redshift range $1.5 < z < 4$. It does not explain the continued growth at lower redshifts where there are few SMGs, which shows that the production of massive early-type galaxies is not entirely the result of the conversion of this seed population.

(vi) We have used our stacking results to show that the ratio of dust-to-stellar mass in galaxies increases with redshift out to $z \sim 8$.

(vii) We have combined our stacking results with the COSMOS-Web stellar mass functions to determine the relationship between the mean density of dust and redshift in the range $0 < z < 12$, extending the work in our earlier paper (S. Eales & B. Ward 2024).

(viii) We have constructed a model for the global evolution of dust in the universe based on the empirical star formation history of the universe and on previous models for the evolution of the metals in galaxies. We show that with a mean gas outflow rate equal to the star formation rate this model reproduces our observed relationship between mean dust density and redshift remarkably well. The model also explains why the mean ratio of dust-to-stellar mass increases monotonically with redshift.

(ix) We use our dust–redshift relationship and assumptions about the evolution of the mean metal abundance in the universe based on recent *JWST* observations to derive the relationship between the mean density of molecular gas and redshift. The shape of this relationship at the lower redshifts ($z < 6$) is similar to the relationship derived using CO rather than dust as the tracer, and the offset can easily be explained in the uncertainties in calibrations of the CO and dust methods.

(x) The relationship we derive between gas density and redshift is, for a gas depletion time of 6.3×10^8 yr, remarkably similar to the star formation history of the universe. The similarity of the two relationships suggests that the global gas depletion time has remained roughly constant over the history of the universe.

ACKNOWLEDGEMENTS

We thank Hiddo Algera, Richard Ellis, Karl Glazebrook, and Ryley Hill for comments on the manuscript. We are particularly grateful to Ian Smail for helping us get rapid access to the S2COSMOS dataset and for his comments on the manuscript, which significantly improved the paper. We are also grateful to an anonymous referee for their careful reading of a very long paper and for many comments which significantly improved it. This work was started while SAE was on a visit to Australia in summer 2025 funded by the Taith fund, Wales' international exchange programme. He thanks Luca Cortese and Karl Glazebrook for helping to arrange his visits, respectively, to the International Centre for Research in Radio Astronomy and Swinburne University. SAE and MWSL are grateful to the Science and Technology Facilities Council (consolidated grant ST/K000926/1) for financial support.

DATA AVAILABILITY

The programs used in this investigation are available on Github (https://github.com/steveales/COSMOS-Web), with the exception of the SIMSTACK program, which can be found at https://github.com/marcoviero/simstack3/tree/main/viero22

REFERENCES

Algera H. S. B. et al., 2026, MNRAS, 545, staf1897
Aoyama S., Hou K.-C., Hirashita H., Nagamine K., Shimizu I., 2018, MNRAS, 478, 4905
Arnouts S., Cristiani S., Moscardini L., Matarrese S., Lucchin F., Fontana A., Giallongo E., 1999, MNRAS, 310, 540
Asano R. S., Takeuchi T. T., Hirashita H., Inoue A. K., 2013, Earth Planets Space, 65, 213
Bakx T. J. L. C. et al., 2018, MNRAS, 473, 1751
Bakx T. J. L. C. et al., 2020, MNRAS, 493, 4294
Bakx T. J. L. C. et al., 2026, MNRAS, 546, stag2284
Barger A. J., Cowie L. L., Sanders D. B., Fulton E., Taniguchi Y., Sato Y., Kawara K., Okuda H., 1998, Nature, 394, 248

Beeston R. A., Gomez H. L., Dunne L., Maddox S., Eales S. A., Smith M. W. L., 2024, MNRAS, 535, 3162
Behrens C., Pallottini A., Ferrara A., Gallerani S., Vallini L., 2018, MNRAS, 477, 552
Bendo G. J. et al., 2023, MNRAS, 522, 2995
Bendo G. J. et al., 2025, MNRAS, 540, 1560
Béthermin M. et al., 2015, A&A, 573, A113
Béthermin M. et al., 2020, A&A, 643, A2
Bolatto A. D., Wolfire M., Leroy A. K., 2013, ARA&A, 51, 207
Bollati F., Lupi A., Dotti M., Haardt F., 2024, A&A, 690, A194
Boselli A. et al., 2010, PASP, 122, 261
Bouwens R. et al., 2020, ApJ, 902, 112
Bouwens R. J. et al., 2022, ApJ, 931, 160
Bruzual G., Charlot S., 2003, MNRAS, 344, 1000
Calura F. et al., 2017, MNRAS, 465, 54
Carnall A. C. et al., 2023a, MNRAS, 520, 3974
Carnall A. C. et al., 2023b, Nature, 619, 716
Casey C. M., Hodge J., Zavala J. A., Spilker J., da Cunha E., Staguhn J., Finkelstein S. L., Drew P., 2018, ApJ, 862, 78
Casey C. M. et al., 2023, ApJ, 954, 31
Casey C. M. et al., 2024, ApJ, 965, 98
Chen C.-C. et al., 2022, ApJ, 939, L7
Cheng C. et al., 2023, ApJ, 942, L19
Clark C. J. R., Schofield S. P., Gomez H. L., Davies J. I., 2016, MNRAS, 459, 1646
Cortese L. et al., 2012, A&A, 540, A52
Croton D. J. et al., 2006, MNRAS, 365, 11
da Cunha E., Charlot S., Elbaz D., 2008, MNRAS, 388, 1595
da Cunha E. et al., 2013, ApJ, 766, 13
da Cunha E. et al., 2021, ApJ, 919, 30
De Cia A., Ledoux C., Mattsson L., Petitjean P., Srianand R., Gavignaud I., Jenkins E. B., 2016, A&A, 596, A97
De Vis P. et al., 2017, MNRAS, 471, 1743
Drew P. M., Casey C. M., 2022, ApJ, 930, 142
Dubois Y., Peirani S., Pichon C., Devriendt J., Gavazzi R., Welker C., Volonteri M., 2016, MNRAS, 463, 3948
Dudzevičiūtė U. et al., 2020, MNRAS, 494, 3828
Dunne L., Eales S. A., 2001, MNRAS, 327, 697
Dunne L. et al., 2011, MNRAS, 417, 1510
Dunne L., Maddox S. J., Papadopoulos P. P., Ivison R. J., Gomez H. L., 2022, MNRAS, 517, 962
Dye S. et al., 2010, A&A, 518, L10
Dye S. et al., 2015, MNRAS, 452, 2258
Dye S. et al., 2022, MNRAS, 510, 3734
Eales S., Ward B., 2024, MNRAS, 529, 1130
Eales S., Lilly S., Gear W., Dunne L., Bond J. R., Hammer F., Le Fèvre O., Crampton D., 1999, ApJ, 515, 518
Eales S. et al., 2012, ApJ, 761, 168
Eales S., de Vis P., Smith M. W. L., Appah K., Ciesla L., Duffield C., Schofield S., 2017, MNRAS, 465, 3125
Eales S. et al., 2018, MNRAS, 473, 3507
Eales S., Gomez H., Dunne L., Dye S., Smith M. W. L., 2024, MNRAS, 532, 2905
Eales S. A., Edmunds M. G., 1996, MNRAS, 280, 1167
Eales S. A., Edmunds M. G., 1997, MNRAS, 286, 732
Eales S. A., Wynn-Williams C. G., Duncan W. D., 1989, ApJ, 339, 859
Edmunds M. G., 1990, MNRAS, 246, 678
Edmunds M. G., Eales S. A., 1998, MNRAS, 299, L29
Ellis R. S., 2025, preprint (arXiv:2508.16948)
Euclid Collaboration, 2025a, preprint (arXiv:2503.15309)
Euclid Collaboration, 2025b, preprint (arXiv:2511.02964)
Euclid Collaboration, 2025c, preprint (arXiv:2511.02989)
Fabian A. C., 2012, ARA&A, 50, 455
Faisst A. L. et al., 2017, ApJ, 847, 21
Faisst A. L. et al., 2020, ApJS, 247, 61
Finkelstein S. L. et al., 2025, ApJ, 983, L4
Ford G. P. et al., 2013, ApJ, 769, 55
Gillman S. et al., 2024, A&A, 691, A299
Glazebrook K. et al., 2017, Nature, 544, 71
Gobat R. et al., 2018, Nat. Astron., 2, 239
Granato G. L., De Zotti G., Silva L., Bressan A., Danese L., 2004, ApJ, 600, 580
Harrington K. C. et al., 2021, ApJ, 908, 95
Hopkins P. F., Cox T. J., Kereš D., Hernquist L., 2008, ApJS, 175, 390
Huertas-Company M. et al., 2025, A&A, 704, A94
Hughes D. H. et al., 1998, Nature, 394, 241
Ismail D. et al., 2023, A&A, 678, A27
Ivison R. J. et al., 2016, ApJ, 832, 78
James A., Dunne L., Eales S., Edmunds M. G., 2002, MNRAS, 335, 753
Jin S. et al., 2019, ApJ, 887, 144
Kelvin L. S. et al., 2014, MNRAS, 444, 1647
Kennicutt R. C. Jr, 1998, ARA&A, 36, 189
Kennicutt R. C. Jr, De Los Reyes M. A. C., 2021, ApJ, 908, 61
Kennicutt R. C., Evans N. J., 2012, ARA&A, 50, 531
Kirkpatrick A. et al., 2017, ApJ, 843, 71
Larson R. B., Tinsley B. M., Caldwell C. N., 1980, ApJ, 237, 692
Le Fèvre O. et al., 2020, A&A, 643, A1
Li Q., Narayanan D., Davé R., 2019, MNRAS, 490, 1425
Liang L. et al., 2019, MNRAS, 489, 1397
Lilly S. J., Carollo C. M., Pipino A., Renzini A., Peng Y., 2013, ApJ, 772, 119
Liu F.-Y. et al., 2026, MNRAS, 545, staf1961
Long A. S., Casey C. M., Lagos C. d. P., Lambrides E. L., Zavala J. A., Champagne J., Cooper O. R., Cooray A. R., 2023, ApJ, 953, 11
Lower S., Narayanan D., Hu C.-Y., Privon G. C., 2024, ApJ, 965, 123
Madau P., Dickinson M., 2014, ARA&A, 52, 415
Magdis G. E. et al., 2012, ApJ, 760, 6
Magdis G. E. et al., 2021, A&A, 647, A33
Magnelli B. et al., 2014, A&A, 561, A86
Magnelli B. et al., 2020, ApJ, 892, 66
Maiolino R., Mannucci F., 2019, A&AR, 27, 3
Marsden G. et al., 2009, ApJ, 707, 1729
Martig M., Bournaud F., Teyssier R., Dekel A., 2009, ApJ, 707, 250
McKinney J. et al., 2025, ApJ, 979, 229
McKinnon R., Torrey P., Vogelsberger M., Hayward C. C., Marinacci F., 2017, MNRAS, 468, 1505
Millard J. S. et al., 2020, MNRAS, 494, 293
Morgan H. L., Edmunds M. G., 2003, MNRAS, 343, 427
Nanayakkara T. et al., 2024, Sci. Rep., 14, 3724
Nanayakkara T. et al., 2025, ApJ, 981, 78
Pearson E. A. et al., 2013, MNRAS, 435, 2753
Peng Y., Maiolino R., Cochrane R., 2015, Nature, 521, 192
Peng Y.-j. et al., 2010, ApJ, 721, 193
Péroux C., Howk J. C., 2020, ARA&A, 58, 363
Planck Collaboration XIII, 2016, A&A, 594, A13
Popesso P. et al., 2023, MNRAS, 519, 1526
Popping G., Somerville R. S., Galametz M., 2017, MNRAS, 471, 3152
Roman-Duval J. et al., 2022a, ApJ, 928, 90
Roman-Duval J. et al., 2022b, ApJ, 935, 105
Saintonge A., Catinella B., 2022, ARA&A, 60, 319
Santini P. et al., 2021, A&A, 652, A30
Schreiber C., Elbaz D., Pannella M., Ciesla L., Wang T., Franco M., 2018, A&A, 609, A30
Scott S. E. et al., 2002, MNRAS, 331, 817
Scoville N. et al., 2007, ApJS, 172, 1
Scoville N. et al., 2014, ApJ, 783, 84
Scoville N. et al., 2016, ApJ, 820, 83
Scoville N. et al., 2017, ApJ, 837, 150
Scoville N. et al., 2023, ApJ, 943, 82
Shuntov M. et al., 2025a, A&A, 704, A339
Shuntov M. et al., 2025b, A&A, 695, A20
Simpson J. M. et al., 2017, ApJ, 839, 58
Simpson J. M. et al., 2019, ApJ, 880, 43
Smail I., Ivison R. J., Blain A. W., 1997, ApJ, 490, L5
Smith M. W. L. et al., 2012, ApJ, 748, 123
Sommovigo L., Algera H., 2025, MNRAS, 540, 3693

Speagle J. S., Steinhardt C. L., Capak P. L., Silverman J. D., 2014, ApJS, 214, 15
Stark D. P., Topping M. W., Endsley R., Tang M., 2026, in Encyclopedia of Astrophysics, Vol. 4. Elsevier, p. 453
Swinbank A. M. et al., 2014, MNRAS, 438, 1267
Tacconi L. J., Genzel R., Sternberg A., 2020, ARA&A, 58, 157
Thomas D., Maraston C., Bender R., Mendes de Oliveira C., 2005, ApJ, 621, 673
Thomas D., Maraston C., Schawinski K., Sarzi M., Silk J., 2010, MNRAS, 404, 1775
Toomre A., Toomre J., 1972, ApJ, 178, 623
Übler H., Naab T., Oser L., Aumer M., Sales L. V., White S. D. M., 2014, MNRAS, 443, 2092
Valentino F. et al., 2020, ApJ, 889, 93
Viero M. P. et al., 2012, MNRAS, 421, 2161
Viero M. P. et al., 2013, ApJ, 779, 32
Viero M. P., Sun G., Chung D. T., Moncelsi L., Condon S. S., 2022, MNRAS, 516, L30
Vijayan A. P., Clay S. J., Thomas P. A., Yates R. M., Wilkins S. M., Henriques B. M., 2019, MNRAS, 489, 4072
Ward B. A., Eales S. A., Ivison R. J., Arumugam V., 2024, MNRAS, 530, 4887
Weingartner J. C., Draine B. T., 2001, ApJ, 548, 296
Whitaker K. E. et al., 2021, Nature, 597, 485
Witstok J., Jones G. C., Maiolino R., Smit R., Schneider R., 2023, MNRAS, 523, 3119
Wuyts S. et al., 2011, ApJ, 742, 96
Zhukovska S., Dobbs C., Jenkins E. B., Klessen R. S., 2016, ApJ, 831, 147

APPENDIX A: FLUX DENSITIES AND MORPHOLOGICAL CLASSIFICATION

The flux densities measured with SIMSTACK shown in Fig. 2 are listed in Table A1. The morphological breakdown of our redshift and stellar mass samples is given in Table A2.

Table A1. Mean flux densities (SIMSTACK).

z_{low}	z_{up}	$\log_{10}(M_{low}/M_\odot)$	$\log_{10}(M_{up}/M_\odot)$	$< S_{850\ \mu m} >$ (mJy)	σ (mJy)
0.2	0.5	9.0	9.5	0.030	0.024
0.2	0.5	9.5	10.0	0.014	0.029
0.2	0.5	10.0	10.5	0.048	0.040
0.2	0.5	10.5	11.0	0.41	0.05
0.2	0.5	11.0	11.5	0.24	0.07
0.5	0.8	9.0	9.5	0.037	0.015
0.5	0.8	9.5	10.0	0.11	0.02
0.5	0.8	10.0	10.5	0.13	0.02
0.5	0.8	10.5	11.0	0.17	0.03
0.5	0.8	11.0	11.5	0.08	0.06
0.8	1.1	9.0	9.5	−0.00	0.01
0.8	1.1	9.5	10.0	0.09	0.01
0.8	1.1	10.0	10.5	0.14	0.02
0.8	1.1	10.5	11.0	0.13	0.02
0.8	1.1	11.0	11.5	0.10	0.05
1.1	1.5	9.0	9.5	−0.02	0.01
1.1	1.5	9.5	10.0	0.04	0.02
1.1	1.5	10.0	10.5	0.16	0.03
1.1	1.5	10.5	11.0	0.32	0.03
1.1	1.5	11.0	11.5	0.52	0.07
1.5	2.0	9.0	9.5	0.036	0.013
1.5	2.0	9.5	10.0	0.070	0.017
1.5	2.0	10.0	10.5	0.26	0.02
1.5	2.0	10.5	11.0	0.38	0.03
1.5	2.0	11.0	11.5	0.66	0.07
2.0	2.5	9.0	9.5	0.027	0.016
2.0	2.5	9.5	10.0	0.12	0.02
2.0	2.5	10.0	10.5	0.39	0.03
2.0	2.5	10.5	11.0	0.82	0.06
2.0	2.5	11.0	11.5	1.45	0.15
2.5	3.0	9.0	9.5	0.01	0.02
2.5	3.0	9.5	10.0	0.17	0.03
2.5	3.0	10.0	10.5	0.49	0.06
2.5	3.0	10.5	11.0	0.73	0.08
2.5	3.0	11.0	11.5	1.30	0.29
3.0	3.5	9.0	9.5	−0.03	0.02
3.0	3.5	9.5	10.0	0.05	0.04
3.0	3.5	10.0	10.5	0.34	0.05
3.0	3.5	10.5	11.0	0.92	0.09

Table A1 – *continued*

z_{low}	z_{up}	$\log_{10}(M_{low}/M_{\odot})$	$\log_{10}(M_{up}/M_{\odot})$	$< S_{850\ \mu m} >$ (mJy)	σ (mJy)
3.0	3.5	11.0	11.5	1.40	0.19
3.5	4.5	9.0	9.5	0.02	0.02
3.5	4.5	9.5	10.0	0.18	0.03
3.5	4.5	10.0	10.5	0.74	0.06
3.5	4.5	10.5	11.0	1.01	0.11
3.5	4.5	11.0	11.5	2.11	0.27
4.5	5.5	9.0	9.5	0.05	0.03
4.5	5.5	9.5	10.0	0.15	0.05
4.5	5.5	10.0	10.5	0.65	0.15
4.5	5.5	10.5	11.0	1.82	0.29
4.5	5.5	11.0	11.5	3.1	0.7
5.5	6.5	9.0	9.5	−0.04	0.05
5.5	6.5	9.5	10.0	0.18	0.10
5.5	6.5	10.0	10.5	0.68	0.30
5.5	6.5	10.5	11.0	2.42	0.52
5.5	6.5	11.0	11.5	2.40	0.77
6.5	7.5	9.0	9.5	0.03	0.06
6.5	7.5	9.5	10.0	0.10	0.12
6.5	7.5	10.0	10.5	0.31	0.26
6.5	7.5	10.5	11.0	0.82	0.59
6.5	7.5	11.0	11.5	1.57	0.80
7.5	8.5	9.0	9.5	0.05	0.09
7.5	8.5	9.5	10.0	0.06	0.11
7.5	8.5	10.0	10.5	0.42	0.25
7.5	8.5	10.5	11.0	1.15	0.59
7.5	8.5	11.0	11.5	2.33	0.85
8.5	12.0	9.0	9.5	−0.13	0.11
8.5	12.0	9.5	10.0	−0.23	0.14
8.5	12.0	10.0	10.5	0.04	0.22
8.5	12.0	10.5	11.0	0.05	0.52
8.5	12.0	11.0	11.5	0.64	0.85

Table A2. Morphological composition.

z_{low}	z_{up}	$\log_{10}(M_{low}/M_{\odot})$	$\log_{10}(M_{up}/M_{\odot})$	Total[a]	Spheroids[a]	Discs[a]	Irregular[a]	Bulge-dominated[a]	Uc[a]
0.2	0.5	9.0	9.5	1798	65 (3 per cent)	725 (40 per cent)	809 (44 per cent)	167 (9 per cent)	32 (1 per cent)
0.2	0.5	9.5	10.0	1026	52 (5 per cent)	522 (50 per cent)	262 (25 per cent)	178 (17 per cent)	12 (1 per cent)
0.2	0.5	10.0	10.5	803	81 (10 per cent)	278 (34 per cent)	99 (12 per cent)	336 (41 per cent)	9 (1 per cent)
0.2	0.5	10.5	11.0	550	82 (14 per cent)	98 (17 per cent)	17 (3 per cent)	350 (63 per cent)	3 (0 per cent)
0.2	0.5	11.0	11.5	113	28 (24 per cent)	8 (7 per cent)	4 (3 per cent)	73 (64 per cent)	0 (0 per cent)
0.5	0.8	9.0	9.5	3837	277 (7 per cent)	1142 (29 per cent)	2139 (55 per cent)	256 (6 per cent)	23 (0 per cent)
0.5	0.8	9.5	10.0	2290	147 (6 per cent)	875 (38 per cent)	986 (43 per cent)	261 (11 per cent)	21 (0 per cent)
0.5	0.8	10.0	10.5	1574	151 (9 per cent)	526 (33 per cent)	408 (25 per cent)	481 (30 per cent)	8 (0 per cent)
0.5	0.8	10.5	11.0	933	133 (14 per cent)	189 (20 per cent)	87 (9 per cent)	518 (55 per cent)	6 (0 per cent)
0.5	0.8	11.0	11.5	210	45 (21 per cent)	8 (3 per cent)	8 (3 per cent)	146 (69 per cent)	3 (1 per cent)
0.8	1.1	9.0	9.5	6812	505 (7 per cent)	1663 (24 per cent)	4272 (62 per cent)	335 (4 per cent)	37 (0 per cent)
0.8	1.1	9.5	10.0	4263	350 (8 per cent)	1241 (29 per cent)	2302 (53 per cent)	350 (8 per cent)	20 (0 per cent)
0.8	1.1	10.0	10.5	2751	324 (11 per cent)	694 (25 per cent)	1139 (41 per cent)	576 (20 per cent)	18 (0 per cent)
0.8	1.1	10.5	11.0	1550	217 (14 per cent)	281 (18 per cent)	306 (19 per cent)	737 (47 per cent)	9 (0 per cent)
0.8	1.1	11.0	11.5	306	69 (22 per cent)	23 (7 per cent)	21 (6 per cent)	190 (62 per cent)	3 (0 per cent)
1.1	1.5	9.0	9.5	6190	318 (5 per cent)	1827 (29 per cent)	3666 (59 per cent)	352 (5 per cent)	27 (0 per cent)
1.1	1.5	9.5	10.0	3652	279 (7 per cent)	1441 (39 per cent)	1584 (43 per cent)	331 (9 per cent)	17 (0 per cent)
1.1	1.5	10.0	10.5	2206	506 (22 per cent)	645 (29 per cent)	647 (29 per cent)	398 (18 per cent)	10 (0 per cent)
1.1	1.5	10.5	11.0	1547	349 (22 per cent)	394 (25 per cent)	180 (11 per cent)	621 (40 per cent)	3 (0 per cent)
1.1	1.5	11.0	11.5	325	86 (26 per cent)	54 (16 per cent)	30 (9 per cent)	155 (47 per cent)	0 (0 per cent)
1.5	2.0	9.0	9.5	8985	530 (5 per cent)	1870 (20 per cent)	6057 (67 per cent)	448 (4 per cent)	80 (0 per cent)
1.5	2.0	9.5	10.0	5020	347 (6 per cent)	1730 (34 per cent)	2421 (48 per cent)	488 (9 per cent)	34 (0 per cent)
1.5	2.0	10.0	10.5	2620	518 (19 per cent)	787 (30 per cent)	939 (35 per cent)	365 (13 per cent)	11 (0 per cent)
1.5	2.0	10.5	11.0	1612	361 (22 per cent)	457 (28 per cent)	260 (16 per cent)	530 (32 per cent)	4 (0 per cent)
1.5	2.0	11.0	11.5	309	68 (22 per cent)	74 (23 per cent)	24 (7 per cent)	143 (46 per cent)	0 (0 per cent)
2.0	2.5	9.0	9.5	6280	305 (4 per cent)	660 (10 per cent)	5067 (80 per cent)	177 (2 per cent)	71 (1 per cent)
2.0	2.5	9.5	10.0	3512	176 (5 per cent)	768 (21 per cent)	2322 (66 per cent)	205 (5 per cent)	41 (1 per cent)
2.0	2.5	10.0	10.5	1894	316 (16 per cent)	389 (20 per cent)	1016 (53 per cent)	151 (7 per cent)	22 (1 per cent)
2.0	2.5	10.5	11.0	934	208 (22 per cent)	169 (18 per cent)	294 (31 per cent)	255 (27 per cent)	8 (0 per cent)
2.0	2.5	11.0	11.5	209	42 (20 per cent)	51 (24 per cent)	38 (18 per cent)	78 (37 per cent)	0 (0 per cent)

Table A2 – *continued*

z_{low}	z_{up}	$\log_{10}(M_{low}/M_{\odot})$	$\log_{10}(M_{up}/M_{\odot})$	Total[a]	Spheroids[a]	Discs[a]	Irregular[a]	Bulge-dominated[a]	Uc[a]
2.5	3.0	9.0	9.5	4202	201 (4 per cent)	248 (5 per cent)	3582 (85 per cent)	72 (1 per cent)	99 (2 per cent)
2.5	3.0	9.5	10.0	2368	126 (5 per cent)	320 (13 per cent)	1790 (75 per cent)	87 (3 per cent)	45 (1 per cent)
2.5	3.0	10.0	10.5	1220	186 (15 per cent)	177 (14 per cent)	775 (63 per cent)	70 (5 per cent)	12 (0 per cent)
2.5	3.0	10.5	11.0	509	120 (23 per cent)	74 (14 per cent)	197 (38 per cent)	114 (22 per cent)	4 (0 per cent)
2.5	3.0	11.0	11.5	106	20 (18 per cent)	22 (20 per cent)	30 (28 per cent)	34 (32 per cent)	0 (0 per cent)
3.0	3.5	9.0	9.5	3154	36 (1 per cent)	41 (1 per cent)	2933 (92 per cent)	4 (0 per cent)	140 (4 per cent)
3.0	3.5	9.5	10.0	1635	63 (3 per cent)	127 (7 per cent)	1384 (84 per cent)	7 (0 per cent)	54 (3 per cent)
3.0	3.5	10.0	10.5	912	110 (12 per cent)	150 (16 per cent)	558 (61 per cent)	24 (2 per cent)	70 (7 per cent)
3.0	3.5	10.5	11.0	473	86 (18 per cent)	123 (26 per cent)	178 (37 per cent)	57 (12 per cent)	29 (6 per cent)
3.0	3.5	11.0	11.5	131	10 (7 per cent)	57 (43 per cent)	22 (16 per cent)	38 (29 per cent)	4 (3 per cent)
3.5	4.5	9.0	9.5	3970	25 (0 per cent)	13 (0 per cent)	3472 (87 per cent)	0 (0 per cent)	460 (11 per cent)
3.5	4.5	9.5	10.0	1823	59 (3 per cent)	77 (4 per cent)	1524 (83 per cent)	8 (0 per cent)	155 (8 per cent)
3.5	4.5	10.0	10.5	873	67 (7 per cent)	131 (15 per cent)	499 (57 per cent)	27 (3 per cent)	149 (7 per cent)
3.5	4.5	10.5	11.0	310	36 (11 per cent)	73 (23 per cent)	94 (30 per cent)	23 (7 per cent)	84 (27 per cent)
3.5	4.5	11.0	11.5	60	2 (3 per cent)	17 (28 per cent)	11 (18 per cent)	9 (15 per cent)	21 (35 per cent)
4.5	5.5	9.0	9.5	2349	11 (0 per cent)	4 (0 per cent)	1972 (83 per cent)	0 (0 per cent)	362 (15 per cent)
4.5	5.5	9.5	10.0	790	13 (1 per cent)	5 (0 per cent)	682 (86 per cent)	0 (0 per cent)	90 (11 per cent)
4.5	5.5	10.0	10.5	201	14 (6 per cent)	5 (2 per cent)	110 (54 per cent)	2 (0 per cent)	70 (34 per cent)
4.5	5.5	10.5	11.0	109	7 (6 per cent)	6 (5 per cent)	19 (17 per cent)	1 (0 per cent)	76 (69 per cent)
4.5	5.5	11.0	11.5	21	0 (0 per cent)	0 (0 per cent)	2 (9 per cent)	0 (0 per cent)	19 (90 per cent)
5.5	6.5	9.0	9.5	972	1 (0 per cent)	0 (0 per cent)	814 (83 per cent)	0 (0 per cent)	157 (16 per cent)
5.5	6.5	9.5	10.0	290	1 (0 per cent)	0 (0 per cent)	254 (87 per cent)	0 (0 per cent)	35 (12 per cent)
5.5	6.5	10.0	10.5	58	1 (1 per cent)	0 (0 per cent)	44 (75 per cent)	0 (0 per cent)	12 (22 per cent)
5.5	6.5	10.5	11.0	28	2 (7 per cent)	4 (14 per cent)	7 (25 per cent)	1 (3 per cent)	14 (50 per cent)
5.5	6.5	11.0	11.5	14	2 (14 per cent)	0 (0 per cent)	3 (21 per cent)	0 (0 per cent)	9 (64 per cent)
6.5	7.5	9.0	9.5	667	2 (0 per cent)	0 (0 per cent)	428 (64 per cent)	0 (0 per cent)	237 (35 per cent)
6.5	7.5	9.5	10.0	198	6 (3 per cent)	0 (0 per cent)	144 (72 per cent)	0 (0 per cent)	48 (24 per cent)
6.5	7.5	10.0	10.5	35	1 (2 per cent)	0 (0 per cent)	21 (60 per cent)	0 (0 per cent)	13 (37 per cent)
6.5	7.5	10.5	11.0	14	1 (7 per cent)	0 (0 per cent)	5 (35 per cent)	0 (0 per cent)	8 (57 per cent)
6.5	7.5	11.0	11.5	9	0 (0 per cent)	0 (0 per cent)	0 (0 per cent)	0 (0 per cent)	9 (100 per cent)
7.5	8.5	9.0	9.5	415	2 (0 per cent)	0 (0 per cent)	220 (53 per cent)	0 (0 per cent)	193 (46 per cent)
7.5	8.5	9.5	10.0	183	9 (4 per cent)	0 (0 per cent)	86 (46 per cent)	0 (0 per cent)	88 (48 per cent)
7.5	8.5	10.0	10.5	25	0 (0 per cent)	0 (0 per cent)	13 (52 per cent)	0 (0 per cent)	12 (48 per cent)
7.5	8.5	10.5	11.0	16	0 (0 per cent)	1 (6 per cent)	5 (31 per cent)	0 (0 per cent)	10 (62 per cent)
7.5	8.5	11.0	11.5	3	0 (0 per cent)	0 (0 per cent)	0 (0 per cent)	0 (0 per cent)	3 (100 per cent)
8.5	12.0	9.0	9.5	128	1 (0 per cent)	0 (0 per cent)	92 (71 per cent)	0 (0 per cent)	35 (27 per cent)
8.5	12.0	9.5	10.0	105	0 (0 per cent)	0 (0 per cent)	71 (67 per cent)	0 (0 per cent)	34 (32 per cent)
8.5	12.0	10.0	10.5	97	0 (0 per cent)	0 (0 per cent)	49 (50 per cent)	1 (1 per cent)	47 (48 per cent)
8.5	12.0	10.5	11.0	26	0 (0 per cent)	0 (0 per cent)	16 (61 per cent)	0 (0 per cent)	10 (38 per cent)
8.5	12.0	11.0	11.5	5	0 (0 per cent)	0 (0 per cent)	2 (40 per cent)	0 (0 per cent)	3 (60 per cent)

Notes. [a]The total is the total number of galaxies in this range of redshift and stellar mass. The numbers in the other columns are the number of galaxies, and in brackets the percentage of the total, in each morphological class. 'Uc' stands for unclassified.

APPENDIX B: BIASES IN THE ESTIMATES OF THE TEMPERATURE OF DUST IN GALAXIES

The dust in a real galaxy has a range of temperatures. The most useful single number that describes the temperature of the dust is probably the mean mass-weighted temperature of the dust, which is what is needed, for example, for an accurate estimate of the mass of the dust.

There is a well-known problem that arises when one estimates the temperature of the dust in a galaxy by fitting a single modified blackbody to its far-IR and submillimetre photometry. The problem arises because warm dust radiates more strongly and at a shorter wavelength than the same mass of cold dust. The effect is that the temperature estimated from fitting the modified blackbody is always higher than the mean mass-weighted temperature of the dust (S. A. Eales et al. 1989). For a given set of observation wavelengths, the difference between the two temperatures – what one measures and what one needs – should increase with redshift as the observations move, in the rest frame of the galaxy, to shorter wavelengths, where the effects of the warm dust are larger. Several groups have investigated this bias using cosmological simulations (C. Behrens et al. 2018; L. Liang et al. 2019; S. Lower et al. 2024; L. Sommovigo & H. Algera 2025). L. Liang et al. (2019), for example, found that although the mean mass-weighted temperature of the dust in their simulations did not increase with redshift, the observed temperature of the dust did.

In this section, we show that even when all the dust in individual galaxies is at the same temperature, the bias is still present when the temperature is estimated from a stacking analysis. The most common way to estimate the dust temperature in a stacking analysis is to measure the mean flux densities of a sample of galaxies at a set of wavelengths and then fit these with a modified blackbody (G. E. Magdis et al. 2012; B. Magnelli et al. 2014; M. Béthermin et al. 2015; C. Schreiber et al. 2018; R. Bouwens et al. 2020; M. P. Viero et al. 2022).

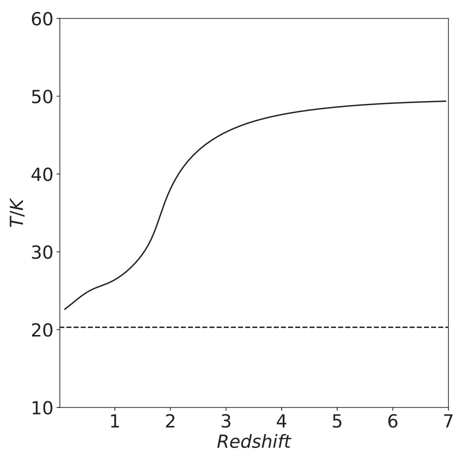

Figure B1. Observed dust temperature versus redshift found from a stacking analysis for a sample of galaxies in which 99 per cent of the galaxies contain dust at 20 K and 1 per cent contain dust at 50 K. The horizontal dashed line show the mean mass-weighted temperature of the dust.

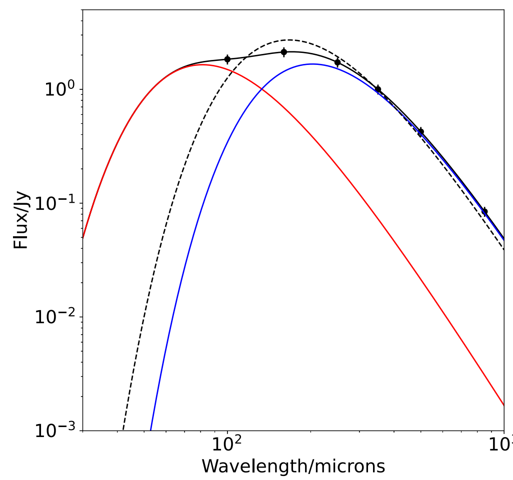

Figure B2. SED (black continuous line) of a sample of galaxies at $z = 3$ for the model described in the text. The red line shows the contribution from the warm ($T = 50$ K) galaxies and the blue line the contribution from the cold ($T = 20$ K) galaxies. The dashed line shows the fit of a modified blackbody at $z = 3$ to mean flux densities (the points and errors) of this sample.

We model this in the following way. We assume that every galaxy contains the same mass of dust with a uniform temperature, with 99 per cent of the galaxies in the sample containing dust at 20 K and the remaining 1 per cent containing dust at 50 K. We assume that the stacking is being carried out at 100, 160, 250, 350, 500, and 850 μm, which are common wavelengths used in stacking analyses. We assume that the sample of galaxies is at a redshift z, calculate the mean flux densities of the sample at each wavelength, and then fit the results with a modified blackbody in the rest frame of the sample. We assume that the value of the emissivity index, β, in the modified blackbody is 2 and that the mean flux densities have 10 per cent errors.

Fig. B1 shows the result. The mean mass-weighted dust temperature is 20.3 K, but the measured dust temperature steadily climbs with redshift, asymptotically approaching the temperature of the warmer galaxies. The explanation for this is the same as the explanation given above for the difference between the observed temperature and the mean mass-weighted dust temperature of individual galaxies. As the redshift increases, the part of the rest-frame SED sampled by the observations will move to shorter wavelengths and the photometry is increasingly dominated by the galaxies with the warmer temperature.

This is illustrated in Fig. B2, which shows the mean SED of a galaxy sample at $z = 3$ in our model and the relative contributions to it of the warm and cold galaxies. At the shortest wavelengths, almost all the flux is contributed by the warm galaxies, even though they only contain 1 per cent of the mass of the dust. The difference between the observed dust temperature and the mean mass-weighted dust temperature increases with redshift as the photometry becomes increasingly dominated by the radiation from the warmer galaxies. One of the most interesting results from a stacking analysis is the recent claim that the dust in galaxies at $z \sim 7$ has a temperature of $\simeq 100$ K (M. P. Viero et al. 2022). Our analysis suggests that the correct interpretation of this result is not that this is the mean temperature of the dust at this redshift, but that some galaxies at this redshift contain dust at this temperature, for which there is evidence from observations of individual galaxies (T. J. L. C. Bakx et al. 2020).

This paper has been typeset from a TEX/LATEX file prepared by the author.